

This is an Open Access document downloaded from ORCA, Cardiff University's institutional repository:<https://orca.cardiff.ac.uk/id/eprint/107253/>

This is the author's version of a work that was submitted to / accepted for publication.

Citation for final published version:

Zhou, Wu, Soultanidis, Nikolaos, Xu, Hui, Wong, Michael S., Neurock, Matthew, Kiely, Christopher J. and Wachs, Israel E. 2017. Nature of catalytically active sites in the supported WO<sub>3</sub>/ZrO<sub>2</sub> solid acid system: a current perspective. *ACS Catalysis* 7 (3) , pp. 2181-2198. 10.1021/acscatal.6b03697

Publishers page: <http://dx.doi.org/10.1021/acscatal.6b03697>

Please note:

Changes made as a result of publishing processes such as copy-editing, formatting and page numbers may not be reflected in this version. For the definitive version of this publication, please refer to the published source. You are advised to consult the publisher's version if you wish to cite this paper.

This version is being made available in accordance with publisher policies. See <http://orca.cf.ac.uk/policies.html> for usage policies. Copyright and moral rights for publications made available in ORCA are retained by the copyright holders.



# Nature of Catalytically Active Sites in the Supported WO<sub>3</sub>/ZrO<sub>2</sub> Solid Acid System: A Current Perspective

Wu Zhou,<sup>†,‡,○,ID</sup> Nikolaos Soultanidis,<sup>§,○,#</sup> Hui Xu,<sup>||</sup> Michael S. Wong,<sup>§,ID</sup> Matthew Neurock,<sup>||,∇</sup> Christopher J. Kiely,<sup>‡,⊥</sup> and Israel E. Wachs<sup>\*,⊥</sup>

<sup>†</sup>School of Physical Sciences, CAS Key Laboratory of Vacuum Sciences, University of Chinese Academy of Sciences, Beijing 100049, People's Republic of China

<sup>‡</sup>Department of Materials Science and Engineering, Lehigh University, Bethlehem, Pennsylvania 18015, United States

<sup>§</sup>Department of Chemical & Biomolecular Engineering, Rice University, Houston, Texas 77005, United States

<sup>||</sup>

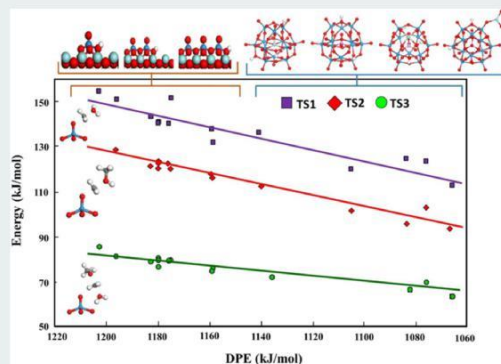
<sup>∇</sup>Department of Chemical and Biomolecular Engineering, Lehigh University, Bethlehem, Pennsylvania 18015, United States

\* Supporting Information

**ABSTRACT:** Tungstated zirconia (WO<sub>3</sub>/ZrO<sub>2</sub>) is one of the most well-studied solid acid catalyst systems and continues to attract the attention of both academia and industry. Understanding and controlling the properties of WO<sub>3</sub>/ZrO<sub>2</sub> catalysts has been a topic of considerable interest over almost the past three decades, with a particular focus on discovering the relationship between catalytic activity and the molecular structure of the surface acid site. Amorphous tungsten oxide (WO<sub>x</sub>) species on ZrO<sub>2</sub> surfaces were previously proposed to be very active for different acidic reactions such as alcohol dehydration and alkane isomerization. Recent developments in electron optical characterization and in situ spectroscopy techniques have allowed researchers to isolate the size, structure, and composition of the most active catalytic species, which are shown to be three-dimensional distorted Zr-WO<sub>x</sub> clusters (0.8–1.0 nm). Complementary theoretical calculations of the Brønsted acidity of these Zr-WO<sub>x</sub> clusters

have confirmed that they possess the lowest deprotonation energy values. This new insight provides a foundation for the future characterization and theory of acidic supported metal oxide catalytic materials that will, hopefully, lead to the design of more active and selective catalysts. This perspective presents an up-to-date, comprehensive summary of the leading models of WO<sub>3</sub>/ZrO<sub>2</sub> solid acid catalysts.

**KEYWORDS:** solid acid catalyst, tungsten oxide, zirconium oxide, mixed W–Zr oxide clusters, spectroscopy, electron microscopy, theory



## 1. INTRODUCTION

Tungstated zirconia (WO<sub>3</sub>/ZrO<sub>2</sub>) catalysts hold considerable promise for being the next generation of solid acid catalysts, and they have attracted considerable research attention since their initial discovery in the late 1980s by Hino and Arata.<sup>1</sup> In their pioneering work, solid acid sites with strengths stronger than that of pure sulfuric acid were obtained on a set of catalysts prepared by impregnation of an aqueous ammonium metatungstate solution onto the surface of an amorphous zirconium oxyhydroxide support, followed by calcination at 800 °C in air.<sup>1</sup> Significantly, these materials were reported to be active for butane and n-pentane isomerization at low temperature (303–323 K)<sup>1</sup> and also show high stability up to 1173 K. The low operational temperature, enhanced regeneration ability, and good thermal stability under H<sub>2</sub>, O<sub>2</sub>, and H<sub>2</sub>O atmospheres exhibited by tungstated zirconia catalysts are all highly desirable characteristics for eventual industrial application.

The desirable solid acid catalytic properties of tungstated zirconia have attracted the attention of numerous researchers in the catalysis community with multiple interests. Tungstated zirconia catalysts have been examined for acid-catalyzed vapor-phase reactions (n-butane isomerization,<sup>2</sup> dehydration of glycerol to acrolein,<sup>3,4</sup> SCR of NO<sub>x</sub> with NH<sub>3</sub>,<sup>5</sup> and SCR of NO<sub>x</sub> with CO<sup>6</sup>) and liquid-phase reactions (esterification of acetic acid with methanol,<sup>7</sup> esterification of acetic acid with 1-heptanol,<sup>8</sup> transesterification of triacetin and methanol,<sup>9</sup> hydration of cyclohexene,<sup>10</sup> synthesis of acetyl salicylic acid,<sup>11</sup> reduction of the viscosity of heavy oil,<sup>12</sup> hydrolysis of cellobiose,<sup>13</sup> fructose conversion into 5-HMF,<sup>14</sup> conversion of glucose to 5-HMF,<sup>15</sup> alkylation of catechol with tert-butyl alcohol,<sup>16</sup> solvent-free acetalization and ketalization,<sup>17</sup> con-

version of cellulose to hexanedione,<sup>18</sup> palmitic acid esterification,<sup>19</sup> synthesis of levulinic acid esters,<sup>20</sup> oxidative desulfurization of thiols,<sup>21</sup> and oxidation of styrene<sup>22</sup>). Additionally, novel syntheses have been reported in an attempt to prepare superior solid acid tungstated zirconia catalysts (mesoporous Zr-WO<sub>x</sub>/SiO<sub>2</sub>,<sup>23</sup> aerogel and xerogel WO<sub>3</sub>/ZrO<sub>2</sub>,<sup>24</sup> mesoporous nano-<sup>17,25,26</sup> MOF-derived tungstated zirconia,<sup>27</sup> two-

WO<sub>x</sub>/ZrO<sub>2</sub>, phase interface hydrolysis,<sup>28</sup> metal oxide promoted WO<sub>x</sub>/ZrO<sub>2</sub>,<sup>5,29-32</sup> precious-metal-promoted WO<sub>x</sub>/ZrO<sub>2</sub>,<sup>6,33-35</sup> and

ZrO<sub>2</sub>-supported tungstaphosphoric acid polyoxometalates<sup>22</sup>). Many of these studies claim that their novel syntheses result in superior tungstated zirconia catalysts. These studies, however, have primarily focused on the use of WO<sub>x</sub>/ZrO<sub>2</sub> solid acid catalysts for numerous applications and have given scant attention to their fundamentals. For the most part, the interpretation of the experimental results has been based on the tungstated zirconia models previously proposed in the literature.

The potential of a promising future of the WO<sub>3</sub>/ZrO<sub>2</sub> catalyst serves as the major motivation to further improve the catalytic performance of this solid acid catalyst system. In order to achieve this goal, the unambiguous identification of the catalytically active site responsible for the enhanced solid acidity of the WO<sub>3</sub>/ZrO<sub>2</sub> catalyst, its molecular and electronic structure, and a more thorough understanding of the structure-activity relationship in this catalyst system is required. Over the past two decades, an extensive variety of catalyst synthesis methods, characterization techniques, and catalytic performance testing studies have been applied to the WO<sub>3</sub>/ZrO<sub>2</sub> catalyst system in an attempt to establish a relationship among the synthesis method, catalyst structure, and catalytic performance.<sup>36-47</sup> In particular, in situ optical spectroscopy techniques (including UV-vis, Raman, and infrared (IR) spectroscopy) have provided invaluable electronic and structural information on the WO<sub>3</sub>/ZrO<sub>2</sub> catalysts at the molecular level. Recently, the application of aberration-corrected scanning transmission electron microscopy (AC-STEM) has further improved the understanding of the catalyst structure at the atomic level and provided a direct means by which to visualize and identify the surface tungsten oxide structures, atom by atom.<sup>44-46,48,49</sup> The combined application of all these advanced characterization techniques has given researchers the capability to gain new insights into the structure-activity relationships about this solid acid catalyst system. General agreement exists that the catalytic activity of the tungstated zirconia catalysts depends on the precise structure of the WO<sub>x</sub> species and their interaction with the zirconia support.<sup>36-47</sup> Specifically, WO<sub>x</sub>-ZrO<sub>x</sub> mixed oxide clusters (hereafter denoted as Zr-WO<sub>x</sub>) that are ~1 nm in size are now thought to be the most effective catalytic materials, comprised of active sites for both alkane isomerization and alcohol dehydration reactions.<sup>44-46</sup>

In this article, we will review the proposed models and recent progress in the study of WO<sub>3</sub>/ZrO<sub>2</sub> catalysts and show how advanced in situ spectroscopy and electron microscopy techniques have been invaluable in understanding the structural details at a molecular level of these complex mixed oxide catalysts, allowing new structure-activity relationships to be developed and providing guidance as to the molecular design of better-performing catalysts. In this perspective we will only discuss the intrinsic structure-activity relationships of un-promoted WO<sub>3</sub>/ZrO<sub>2</sub> catalysts, although it has been noted that the activity and isomerization selectivity of the catalysts can be

further increased by promotion with Pt and some transition-metal oxides (e.g., FeO<sub>x</sub>).<sup>50-55</sup> It should be emphasized that the WO<sub>3</sub>/ZrO<sub>2</sub> system shares many common characteristics with supported oxide-on-oxide catalyst systems, including a strong wetting interaction, which is one of the major factors that controls the surface structures inherent to these materials. The research methodology described in this article, thus, is also generally applicable to uncovering the structure-activity relationships for other oxide-on-oxide catalyst systems.

## 2. DETERMINATION OF THE STRUCTURE-ACTIVITY RELATIONSHIPS

2.1. Effects of Synthesis Parameters on Catalytic Activity. Most of the tungstated zirconia catalysts reported in the literature have been synthesized by the aqueous impregnation<sup>1, 38, 44, 46</sup> of ammonium metatungstate ((NH<sub>4</sub>)<sub>10</sub>W<sub>12</sub>O<sub>41</sub>·5H<sub>2</sub>O) onto a zirconia support, followed by calcination at high temperature. Two different types of zirconia supports are commonly used: amorphous zirconium oxy-hydroxide (ZrO<sub>x</sub>(OH)<sub>4-2x</sub>) and crystalline zirconia (ZrO<sub>2</sub>). Several parameters, including the nature of the ZrO<sub>2</sub> support precursor, the WO<sub>3</sub> loading (employing ammonium metatungstate), and the calcination temperature, seem to have a significant effect on the performance of the final catalytic materials. Understanding how each synthesis parameter affects the catalytic performance can serve to help optimize the preparation procedure and achieve better catalytic performance.

2.1.1. Effect of Crystallinity and Polymorphic Structure of the ZrO<sub>2</sub> Support on the Acidic Catalytic Activity. In their original paper,<sup>1</sup> Hino and Arata observed that WO<sub>x</sub> supported on zirconium oxyhydroxide was active for alkane isomerization, while strong acid sites cannot be readily generated on a crystalline ZrO<sub>2</sub> support. This was subsequently confirmed by studies from many other groups.<sup>36,38,44,56,57</sup> Lebarbier et al.<sup>58</sup> proposed that, for a given W surface density (W atoms/nm<sup>2</sup>), the catalytic performance is mainly controlled by the tetragonal to monoclinic volume fraction ratio of the ZrO<sub>2</sub> structural polymorphs comprising the support rather than their amorphous or crystalline nature. Two different support materials, namely amorphous zirconium oxyhydroxide and "crystalline ZrO<sub>2</sub>", were examined by Lebarbier et al., and they were impregnated with varying amounts of ammonium metatungstate and calcined at 1073 K. By correlating the crystal structure of the ZrO<sub>2</sub> support as determined from X-ray diffraction (XRD) and the catalytic activities of these two series of catalysts, Lebarbier et al.<sup>58</sup> concluded that, for the same WO<sub>x</sub> surface density, both series of catalysts gave rise to a similar tetragonal ZrO<sub>2</sub> volume fraction and catalytic performance. It should be noted, however, that the "crystalline ZrO<sub>2</sub>" support used by these researchers was made by calcination of an amorphous zirconium oxyhydroxide at a relatively mild temperature (773 K) and that unambiguous evidence for the fully crystalline nature of this support cannot be determined by XRD. Indeed, the "crystalline ZrO<sub>2</sub>" support used in the Lebarbier et al. study exhibited a very high surface area of 108 m<sup>2</sup>/g (i.e., equivalent to an average particle size of ~10 nm), indicating that the material may not be fully crystalline.

In order to clarify the effect of the ZrO<sub>2</sub> support, Ross-Medgaarden et al.<sup>44</sup> performed similar experiments on amorphous ZrO<sub>x</sub> and a series of heat-treated "fully" crystalline ZrO<sub>2</sub> support materials. By plotting the catalytic performance as a function of crystal polymorph ratio for the two sets of catalysts (i.e., derived initially from (i) amorphous ZrO<sub>x</sub> and

(ii) crystalline ZrO<sub>2</sub> supports), Ross-Medgaarden et al.<sup>44</sup> demonstrated that there is no direct correlation between the catalytic activity and the tetragonal to monoclinic ratio of the ZrO<sub>2</sub> structural polymorphs comprising the zirconia support materials (Figure 1). Moreover, the catalysts prepared from the

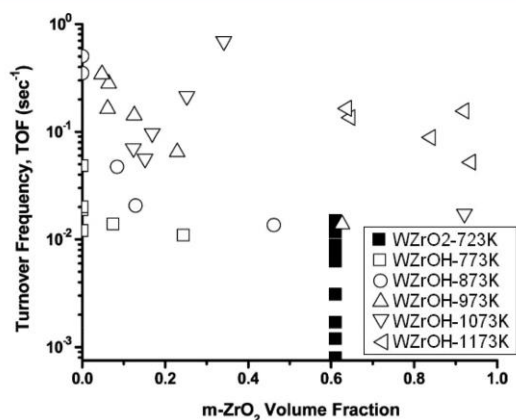


Figure 1. Methanol dehydration catalytic activity (in terms of turnover frequency, TOF) as a function of monoclinic-ZrO<sub>2</sub> (m-ZrO<sub>2</sub>) volume fraction over two series of WO<sub>3</sub>/ZrO<sub>2</sub> catalysts. WZrOH catalysts were synthesized using an amorphous (ZrO<sub>x</sub>(OH)<sub>4-2x</sub>) support and were calcined at different temperatures, whereas WZrO<sub>2</sub> catalysts were synthesized using heat-treated crystalline ZrO<sub>2</sub> support and were calcined at 723 K. Steady-state CH<sub>3</sub>OH dehydration reaction conditions: 573 K, 1 atm, 6% CH<sub>3</sub>OH, 12% O<sub>2</sub> in He and overall CH<sub>3</sub>OH conversion <10%. Adapted from ref 44.

amorphous (ZrO<sub>x</sub>(OH)<sub>4-2x</sub>) support systematically displayed a higher catalytic activity level in comparison to those from the initially well crystallized ZrO<sub>2</sub> supports, suggesting that the initial presence of amorphous ZrO<sub>x</sub> plays an important role in developing good activity in the final WO<sub>3</sub>/ZrO<sub>2</sub> catalysts. The crucial role of amorphous ZrO<sub>x</sub> was later determined to be related to the formation of the most active catalytic sites in this catalyst system (i.e., the Zr-WO<sub>x</sub> mixed oxide clusters), in which the Zr<sup>4+</sup> cations are supplied by the amorphous (ZrO<sub>x</sub>(OH)<sub>4-2x</sub>) support.<sup>44-46</sup> Due to the high catalytic activity of the WO<sub>3</sub>/ZrO<sub>2</sub> catalysts derived from amorphous ZrO<sub>x</sub>, the remaining discussion will focus primarily on these high-activity catalysts, while the model WO<sub>3</sub>/ZrO<sub>2</sub> catalysts derived from initially crystalline ZrO<sub>2</sub> supports will be used only for comparative purposes. It also needs to be emphasized that solid acid catalysis is a surface phenomenon that does not involve the zirconia bulk phase and, consequently, catalytic performance should not correlate with bulk properties.

**2.1.2. Interplay between Tungsten Oxide Loading and the Final Form of the ZrO<sub>2</sub> Support.** By systematic changes in the synthesis parameters, it was noticed that there is a strong interplay between the tungsten oxide loading and calcination temperature in determining the structural characteristics of the ZrO<sub>2</sub> support: namely, (i) the surface area and (ii) the volume

amorphous ZrO<sub>x</sub>(OH)<sub>4-2x</sub> is used as the support precursor and impregnated with WO<sub>x</sub> species, it was found that the WO<sub>x</sub> species can strongly influence the crystallization of the ZrO<sub>2</sub> support. As shown in Figure 2A,B, the addition of tungsten oxide to the ZrO<sub>2</sub> support can help to stabilize the metastable tetragonal ZrO<sub>2</sub> polymorph and retard the sintering of ZrO<sub>2</sub> at high temperatures. For a given calcination temperature, both

the volume fraction of the tetragonal ZrO<sub>2</sub> phase and the surface area of the catalyst increase with an increasing tungsten oxide loading and level off at high loadings when bulk WO<sub>3</sub> crystals begin to form (Figure 2C,D). This stabilization effect was attributed to the strongly bound surface WO<sub>x</sub> species, which can hinder the rate of the ZrO<sub>2</sub> surface diffusion and thus inhibit the growth of ZrO<sub>2</sub> particles.<sup>37</sup> This effect becomes less significant at very high calcination temperatures when the surface WO<sub>x</sub> species agglomerate into bulk WO<sub>3</sub> crystals. Consequently, for a catalyst with a given WO<sub>x</sub> surface density, the ZrO<sub>2</sub> crystallite phase and high surface area can, in principle, be controlled by carefully tuning the tungsten oxide loading and the calcination temperature.

### 2.1.3. Dependence of the Activity of WO<sub>3</sub>/ZrO<sub>2</sub> Catalysts on the Surface WO<sub>x</sub> Density and Calcination Temperature.

In general, the catalytic activity of the final WO<sub>3</sub>/ZrO<sub>2</sub> catalyst can be quite sensitive to the calcination temperature and the concentration of the active component (in this case tungsten oxide). In early studies, it was noticed that, for a given tungsten concentration, the maximum achievable catalytic activity displays a strong dependence on calcination temperature, with the optimum temperature being in the range of 900–1200

K (~600–900 °C) depending on the precise tungsten oxide weight loading<sup>1,37</sup> (Figure 3A). Similarly, for a given calcination temperature, there also seems to be an optimum “intermediate” tungsten oxide concentration<sup>37,55</sup> that gives rise to the best catalytic activity (Figure 3B). It should be noted, however, that the specific surface area of the catalyst also depends on both the calcination temperature and the tungsten oxide loading. It was found that when the tungsten oxide loading is normalized by the final surface area of the catalyst (i.e., obtaining the surface W/nm<sup>2</sup> density), the catalytic activity displays a sole dependence on the W surface density (Figure 4) for reactions such as methanol dehydration,<sup>44</sup> o-xylene isomerization,<sup>37</sup> and 2-butanol dehydration<sup>40</sup> and a dual dependence on surface density and calcination temperature (Figure 5) for reactions such as n-pentane isomerization<sup>36,46</sup> and acetic acid ester-ification.<sup>59</sup> The strong surface density dependence seen in all cases indicates that the surface structures of tungsten oxide on ZrO<sub>2</sub> are primarily controlled by the surface W density. This is only true if there is a relatively strong affiliation between the two oxide components and if the distribution of tungsten oxide on the surface can quickly reach thermodynamic equilibrium under the high-temperature synthesis conditions investigated. In section 2.3.4 it will be demonstrated that there is indeed a strong wetting interaction between WO<sub>x</sub> species and the surface of ZrO<sub>2</sub>, as revealed by detailed optical spectroscopy and electron microscopy characterization.

Comparison of the 2-butanol dehydration and o-xylene isomerization activities (Figure 4) shows that the maximum activity shifts from ~9.5 W/nm<sup>2</sup> for the former to ~7.5 W/nm<sup>2</sup> for the latter, respectively. Even though, as will be discussed later, the distribution of the amorphous WO<sub>x</sub> species on the surface does not change drastically between 8 and 10 W/nm<sup>2</sup>, there is still a direct specific probe molecule–catalytic activity correlation.

The calcination temperature employed has an additional effect on the n-pentane isomerization activity of WO<sub>3</sub>/ZrO<sub>2</sub> materials (Figure 5). When the calcination temperature was increased from 773 to 973 K, the n-pentane isomerization activity was found to increase by a factor of 10 at a loading of ~5.2 W/nm<sup>2</sup> (Figure 5A).<sup>46</sup> Scheithauer et al. have also reported a similar calcination temperature effect.<sup>36</sup> When their

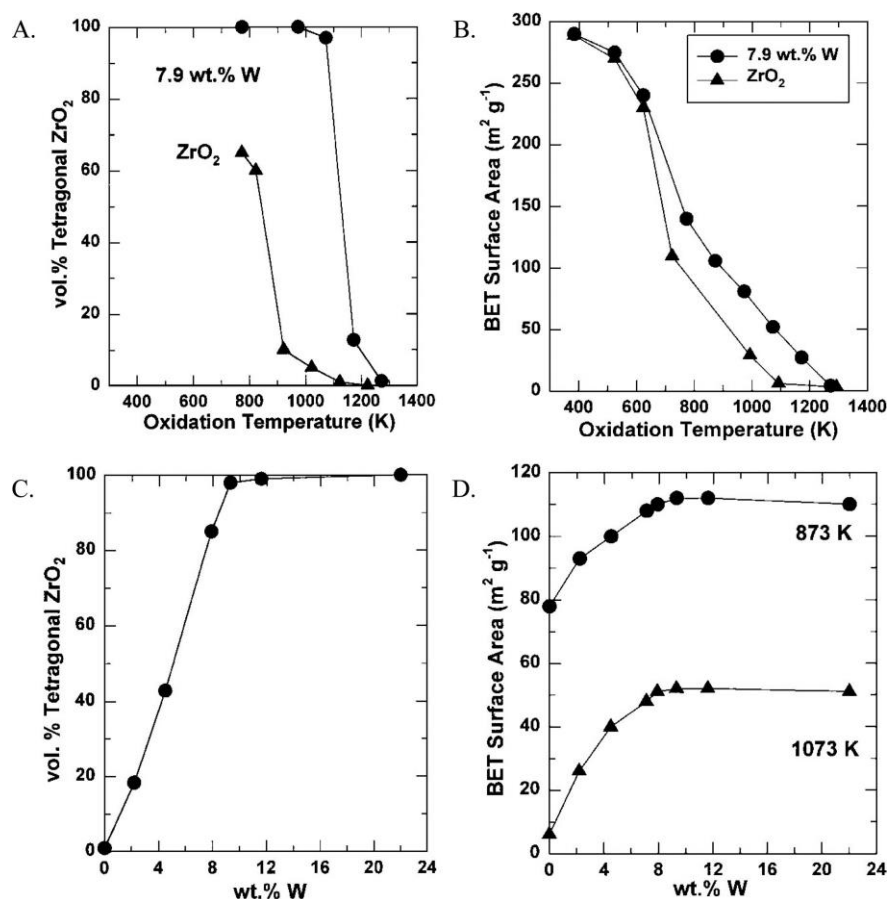


Figure 2. Tetragonal ZrO<sub>2</sub> polymorph volume fraction (A) and BET surface area (B) of pure ZrO<sub>2</sub> and a 7.9 wt % WO<sub>3</sub>/ZrO<sub>2</sub> material as a function of calcination temperature. (C) Tetragonal ZrO<sub>2</sub> polymorph volume fraction of a series of WO<sub>3</sub>/ZrO<sub>2</sub> materials calcined at 1073 K as a function of WO<sub>3</sub> loading. (D) BET surface area data for two series of WO<sub>3</sub>/ZrO<sub>2</sub> materials calcined at 873 and 1073 K, respectively, as a function of WO<sub>3</sub> loading. Adapted from ref 37.

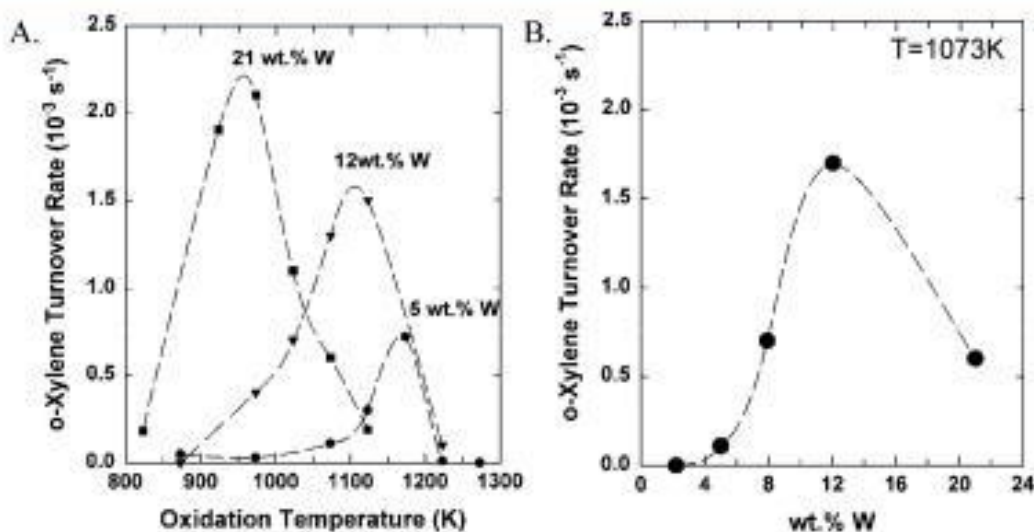


Figure 3. o-Xylene isomerization turnover rates (per W atom) (A) as a function of calcination temperature for different tungsten oxide concentrations and (B) as a function of tungsten oxide concentration at the same calcination temperature (1073 K). o-Xylene isomerization conditions: 523 K, 0.67 kPa o-xylene, 106 kPa H<sub>2</sub> or He, and o-xylene conversion <2%. Adapted from ref 37.

published data is replotted in terms of surface W density, a maximum activity occurs at  $\sim 5$  W/nm<sup>2</sup> and the activity drops by a factor of 2 when the calcination temperature is increased from 923 to 1098 K.

For the quantification of catalytic activity, it is important to note that two different approaches are currently employed in reporting the catalytic activity. Generally, the catalytic activity can be expressed as (i) the reaction rate per gram or atom of

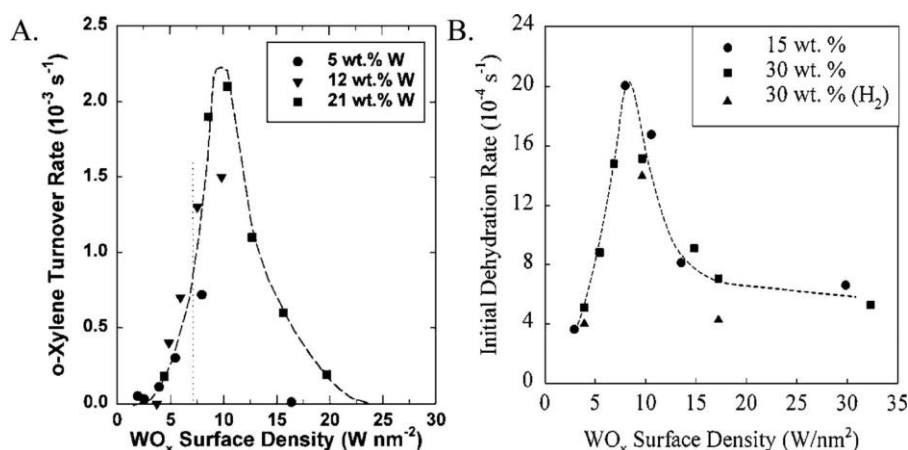


Figure 4. Turnover rates (per W atom) as a function of  $\text{WO}_x$  surface density on  $\text{WO}_3/\text{ZrO}_2$  catalysts for (A) the *o*-xylene isomerization reaction and (B) the 2-butanol dehydration reaction. *o*-Xylene isomerization conditions: 523 K, 0.67 kPa *o*-xylene, 106 kPa  $\text{H}_2$  or He, and *o*-xylene conversion <2% (adapted from ref 37). Initial 2-butanol dehydration rate conditions: 373 K, 0.8 kPa 2-butanol, 100 kPa  $\text{H}_2$  or He, and 2-butanol conversion 1–50% (adapted from ref 40).

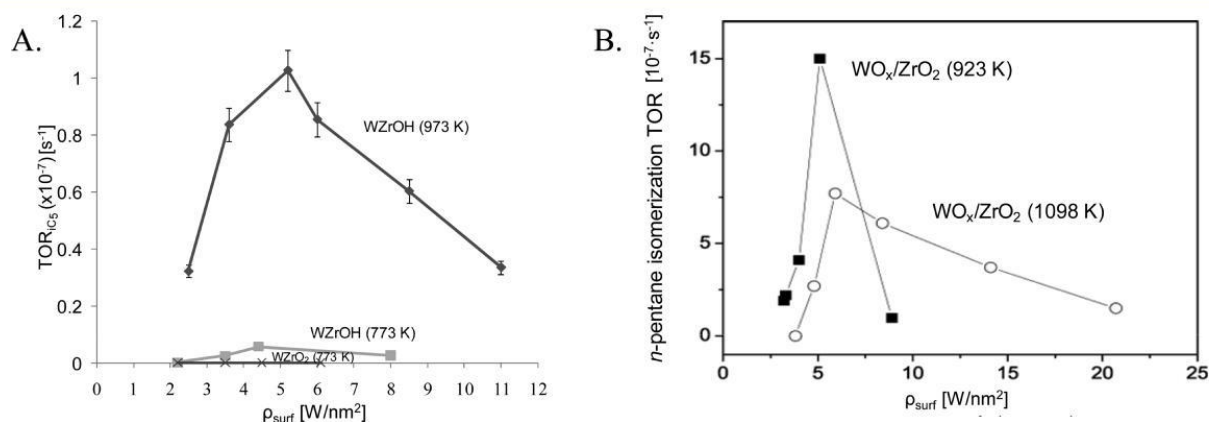


Figure 5. (A) Turnover rates (per W atom) as a function of  $\text{WO}_x$  surface density on  $\text{WO}_3/\text{ZrO}_2$  catalysts for steady-state *n*-pentane isomerization (after 10 h reaction time). Steady-state *n*C<sub>5</sub> isomerization reaction conditions: 523 K, 1.04 atm, 1% *n*C<sub>5</sub> in He. The overall *n*C<sub>5</sub> conversion is <3% (adapted from ref 46). (B) Maximum *n*-pentane isomerization after the induction period. *n*C<sub>5</sub> isomerization reaction conditions: 523 K, 1.01 bar, 0.01 bar *n*C<sub>5</sub> in  $\text{N}_2$ . Note that Figure 5B has been modified from the original published version in ref 36: it has been replotted as surface  $\text{WO}_x$  density versus activity expressed in terms of the *n*-pentane TOR.

the active component or (ii) the reaction rate per catalytically active site under the given reaction conditions. When the reaction rate is normalized by the total loading of the active component, it is usually referred as turnover rate (TOR): i.e., the number of reactant molecules reacted per active component atom per second. This particular quantification method is commonly used in the catalysis literature<sup>36,37,39,40,56</sup> (see Figures 3–5 for example) and serves as a simple and reasonable method for measuring the catalytic activity when the active component is 100% dispersed or exposed on the catalyst surface. The catalytic activity of the surface active sites, however, can be significantly underestimated by the TOR method when large particles of the active component are formed in the catalyst, since catalytic reactions only take place on exposed surface sites in such heterogeneous solid catalysts.<sup>43</sup>

A more reliable and meaningful quantification method incorporates the concept of turnover frequency (TOF; i.e. the number of reactant molecules reacted per exposed catalytically active site per second) as championed by Boudart,<sup>60</sup> where the reaction rate is normalized by the number of exposed catalytically active sites on the catalyst surface. The number of catalytically active sites in the catalyst

can be measured using the temperature-programmed surface reaction (TPSR) spectroscopy method, which only probes the exposed sites.<sup>43,44</sup>

The TOF values can deviate considerably from the TOR value if the dispersion of the catalytically active component is poor.<sup>43</sup> One example of the consequences of switching between the different TOF and TOR metrics is shown in Figure 6 for data taken from a set of model  $\text{WO}_3/\text{ZrO}_2$  catalysts (using a well-crystallized  $\text{ZrO}_2$  support).<sup>43</sup> The TOF values are calculated on the basis of the exposed catalytic sites, which is considered to be the true measurement of catalytic activity and can be readily used for comparative purposes between different catalyst samples. Reporting the catalytic activity as TOR results in a maximum in rate that is not reflected when the catalytic activity is reported as TOF. The reason for the maximum rate in the TOR plot is that  $\text{WO}_3$  particles are present at higher tungsten oxide loadings and the TOR approach does not discriminate between exposed and bulk  $\text{WO}_x$  sites and normalizes the rate by all  $\text{WO}_x$  sites in the catalyst. Consequently, the TOR values will eventually decrease, since most of the  $\text{WO}_x$  sites are in the bulk and do not participate in the catalytic reaction. The TOF approach normalizes the rate

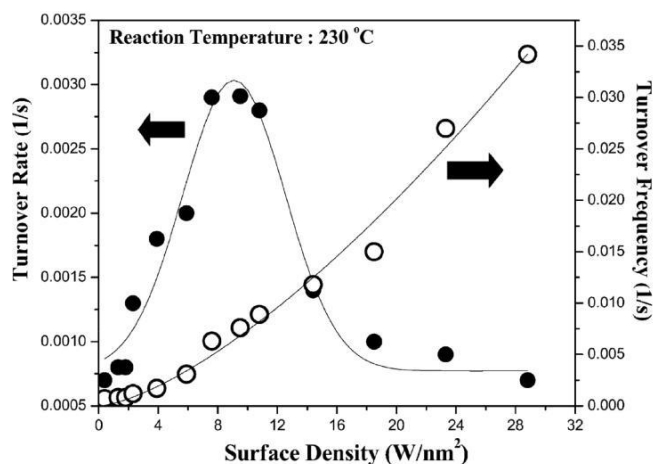


Figure 6. Comparison of catalytic activity for methanol dehydration to dimethyl ether in terms of TOR (solid symbols) and TOF (open symbols) for the same series of model-supported  $\text{WO}_3/\text{ZrO}_2$  catalysts as a function of tungsten oxide surface density. Adapted from ref 43.

by only exposed sites and, therefore, does not exhibit this artificial maximum in catalytic activity. As the catalytic activity is strongly affected by the surface structure of the catalyst, utilizing the TOF value as an indication of the catalytic activity in establishing the structure-activity relationship is considered to be the better approach for quantifying catalytic activity.<sup>60</sup>

**2.2. Monolayer Coverage of  $\text{WO}_x$  on the  $\text{ZrO}_2$  Support Surface.** Given that the catalytic activity of  $\text{WO}_3/\text{ZrO}_2$  solid acid catalysts strongly depends on the surface  $\text{WO}_x$  density, it is important to characterize the structure of the catalysts as a function of this parameter. The concept of monolayer coverage is widely used in supported metal oxide catalyst research to describe the maximum dispersion of the active oxide phase on the support surface. By definition, a monolayer is a single closely packed layer of atoms or molecules on a surface.<sup>61</sup> Below monolayer coverage, the active metal oxide components are generally expected to be highly dispersed on the support surface as isolated (also known as monotungstates) or polymeric (also known as polytungstates) species (e.g., 1D and 2D surface  $\text{WO}_x$ ) with single atomic layer thickness.<sup>38</sup> These submonolayer structures will be discussed further in section 2.3. Above monolayer coverage, the  $\text{WO}_3$  crystalline phase (e.g., 3D nanoparticles (NPs)) of the active metal oxide component usually forms on the surface of the sup-

<sup>36,38,42,43</sup>

port. Therefore, the idea of a

monolayer coverage

value has been used primarily as a benchmark in the quantitative investigation of the surface structure of oxide overlayers as a function of surface density.<sup>36,38,56</sup> Three main approaches have been employed to determine surface  $\text{WO}_x$  monolayer coverage on  $\text{ZrO}_2$ : namely, (1) an experimental determination of the transition from 2D surface  $\text{WO}_x$  species to 3D  $\text{WO}_3$  NPs using physical probes, (2) chemical probe studies, and (3) calculations based on hypothetical surface  $\text{WO}_x$  structures.

**2.2.1. Physical Probes.** The transition from 2D surface  $\text{WO}_x$  species to 3D  $\text{WO}_3$  NPs is best determined by Raman spectroscopy because of its excellent sensitivity to both surface tungsten oxide species and 3D  $\text{WO}_3$  NPs. The normalized intensity of the Raman signals for the surface  $\text{WO}_x$  species and crystalline  $\text{WO}_3$  NPs are plotted in Figure 7 as a function of surface W density ( $\text{W}/\text{nm}^2$ ) on a model crystalline m- $\text{ZrO}_2$  support.<sup>43</sup> The intensity of the Raman band for the surface

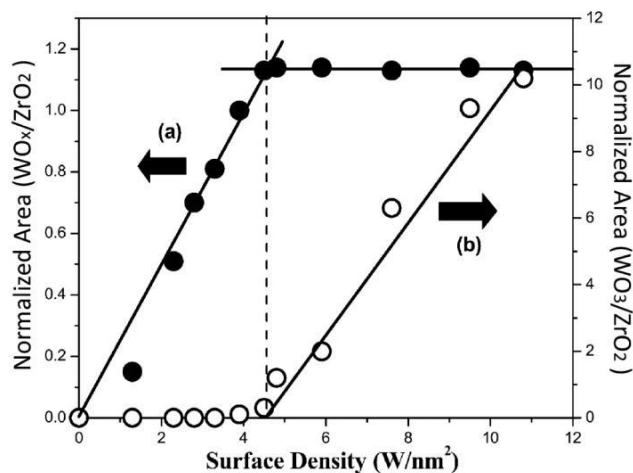


Figure 7. Normalized Raman intensity of the dehydrated surface  $\text{WO}_x$  species ( $\sim 1000\text{--}1020\text{ cm}^{-1}$ ) and crystalline  $\text{WO}_3$  particles ( $\sim 805\text{ cm}^{-1}$ ) as a function of tungsten oxide surface density on a series of model supported  $\text{WO}_3/\text{ZrO}_2$  catalysts. Normalization was performed against the  $471\text{ cm}^{-1}$  band of the  $\text{ZrO}_2$  support. The dashed line indicates the surface density corresponding to monolayer coverage at  $\sim 4.5\text{ W}/\text{nm}^2$  (adapted from ref 43).

$\text{WO}_x$  species increases linearly with tungsten surface density up to  $\sim 4.5\text{ W}/\text{nm}^2$  and then levels off once the surface of the  $\text{ZrO}_2$  support is saturated with surface  $\text{WO}_x$  species (i.e., indicating that monolayer coverage is attained). Above  $4.5\text{ W}/\text{nm}^2$ , the intensity of the Raman signal for the 3D  $\text{WO}_3$  NPs increases linearly with tungsten surface density. Barton et al.<sup>38</sup> also showed that, for active  $\text{WO}_3/\text{ZrO}_2$  catalysts, the ratio of the intensity of the Raman bands for  $\text{WO}_3/\text{WO}_x$  begins to increase linearly starting at  $4.0\text{ W}/\text{nm}^2$ , indicating that monolayer coverage corresponds to  $\sim 4.0\text{ W}/\text{nm}^2$ . XPS surface analysis is another physical characterization technique that discriminates between the 2D surface  $\text{WO}_x$  phase and the 3D  $\text{WO}_3$  NPs due to the different signal responses to the 2D and 3D phases.<sup>47</sup> The XPS transition from 2D to 3D behavior occurs at  $\sim 5\text{ W}/\text{nm}^2$  for active  $\text{WO}_3/\text{ZrO}_2$  catalysts prepared from amorphous zirconia hydroxide.<sup>47</sup> One study also attempted to employ UV-vis spectroscopy to determine monolayer loading coverage for supported  $\text{WO}_3/\text{ZrO}_2$  catalysts.<sup>38</sup> The UV-vis optical edge energy ( $E_g$ ), which reflects the  $\text{WO}_x$  domain size, however, is not particularly sensitive to the 2D to 3D structural transition occurring at monolayer coverage, as the  $E_g$  value continuously decreases with increasing tungsten oxide loading. Only by combining UV-vis measurements with other spectroscopic studies can the 2D to 3D transition be accurately determined.<sup>43,47</sup> Although XRD has also been used to detect the appearance of relatively large 3D  $\text{WO}_3$  NPs, it is unable to detect  $\text{WO}_3$  crystallites smaller than  $\sim 3\text{ nm}$  that nucleate at the 2D to 3D transition at monolayer surface coverage. It is, therefore, not surprising that XRD only begins to detect 3D  $\text{WO}_3$  NPs at loadings of  $6.2\text{ W}/\text{nm}^2$ , which is much greater than the  $4\text{--}5\text{ W}/\text{nm}^2$  value determined with the more sensitive Raman, XPS, and IR spectroscopy techniques.<sup>62</sup> Thus, most applicable experimental spectroscopic measurements agree that monolayer coverage of surface  $\text{WO}_x$  species on  $\text{ZrO}_2$  supports corresponds to  $4\text{--}5\text{ W}/\text{nm}^2$ , with a value of  $\sim 4.5\text{ W}/\text{nm}^2$  being typical for model  $\text{WO}_3/\text{ZrO}_2$  catalysts.

**2.2.2. Chemical Probes.** The nature of the exposed surface sites for the  $\text{WO}_3/\text{ZrO}_2$  catalyst system can also be determined with molecular chemical probes.<sup>39,63,64</sup> Chemisorption of CO at

77 K on supported WO<sub>3</sub>/ZrO<sub>2</sub> catalysts chemically probes exposed Zr sites, and IR spectroscopy reveals that CO surface coverage reaches a minimum at 4.7 W/nm<sup>2</sup> because the surface WO<sub>x</sub> monolayer essentially covers the majority of exposed sites on the ZrO<sub>2</sub> support.<sup>64</sup> Chemisorption of CO<sub>2</sub> also titrates the basic zirconia sites, and IR spectroscopy reveals that CO<sub>2</sub> surface coverage reaches a minimum at ~4.5 W/nm<sup>2</sup>.<sup>38,39,63</sup> Although it is somewhat difficult to determine monolayer surface WO<sub>x</sub> coverage from just UV-vis DRS of the oxidized catalysts, it is possible to discriminate between reducible and irreducible supported tungsten oxide species on ZrO<sub>2</sub> with UV-vis spectroscopy. Reduction studies of supported WO<sub>3</sub>/ZrO<sub>2</sub> catalysts using H<sub>2</sub> treatments revealed that the tungsten oxide species, when present at a coverage below 4.1 W/nm<sup>2</sup>, do not reduce under the chosen experimental conditions, whereas tungsten oxide species that exist above this 4.1 W/nm<sup>2</sup> surface density are reducible.<sup>38</sup> This transition from irreducible to reducible tungsten oxide species was originally assigned to the transition from mono- to polytungstate surface WO<sub>x</sub> species on the ZrO<sub>2</sub> support<sup>38</sup> but actually corresponds to the transition from 2D surface WO<sub>x</sub> species to 3D WO<sub>3</sub> NPs, as revealed in the corresponding Raman spectra presented in the same study.<sup>38</sup>

**2.2.3. Hypothetical Surface WO<sub>x</sub> Structures.** The surface W density for WO<sub>x</sub> monolayer coverage has also been estimated by invoking the structures of the WO<sub>x</sub> species present on the ZrO<sub>2</sub> surface. By assuming that the surface WO<sub>x</sub> oxyanions are present as WO<sub>4</sub><sup>2-</sup> monotungstates anchored to the ZrO<sub>2</sub> surface, it was estimated that monolayer coverage would correspond to ~3.6 W/nm<sup>2</sup>.<sup>57</sup> Another study estimated the theoretical monolayer coverage to be ~4.3 W/nm<sup>2</sup>, assuming a two-dimensional close-packing model where one WO<sub>x</sub> monomeric structural unit occupies 23 Å<sup>2</sup>.<sup>65</sup> On the basis of the dimension of WO<sub>6</sub> units present in the crystalline WO<sub>3</sub> bulk structure, however, a much higher monolayer surface coverage of ~7 W/nm<sup>2</sup> was estimated.<sup>37</sup> The problems with such hypothetical estimates for the surface WO<sub>x</sub> density at monolayer coverage are that (1) idealized surface WO<sub>x</sub> structures are assumed that are not representative of the actual surface WO<sub>x</sub> species on ZrO<sub>2</sub> (see sections below) and (2) the anchoring mode of the surface WO<sub>x</sub> species onto the ZrO<sub>2</sub> support is completely ignored. For instance, the number of W-O-Zr bonds and the respective bond lengths of the different functionalities (W-O, W-O-W, and W-O-Zr) are not taken into account and neither are the potential effects of steric hindrance and lateral repulsion between neighboring surface WO<sub>x</sub> species.<sup>38,39,64,66,67</sup>

The various “monolayer surface coverage” values for WO<sub>x</sub>/ZrO<sub>2</sub> catalysts reported in the literature are summarized in Table 1, and a more detailed review of this particular issue has recently been published.<sup>68</sup> The experimentally determined values are in general agreement that surface WO<sub>x</sub> monolayer coverage on ZrO<sub>2</sub> corresponds to ~4–5 W/nm<sup>2</sup>, with the mean value being ~4.5 W/nm<sup>2</sup>. The only two experimental studies that report unusually high surface WO<sub>x</sub> monolayer coverage values (6.2 and 7 W/nm<sup>2</sup>) employed characterization methods (XRD and UV-vis) that are not sensitive to the specific structures of the supported tungsten oxide phase.

**2.3. Identification of the Acidic Catalytic Active Sites of Supported WO<sub>3</sub>/ZrO<sub>2</sub> Catalysts.** One of the key issues in catalysis research is to identify the structure of the catalytically active sites responsible for the chemical reaction of interest. It has been reported that a variety of different structures of the

Table 1. Summary of Monolayer Surface Coverage Values Reported in the Literature for Supported WO<sub>3</sub>/ZrO<sub>2</sub> Catalysts

monolayer coverage (W/nm <sup>2</sup> )	method	ref
3.6–4.3 <sup>a</sup>	theoretical calculation (assumes isolated WO <sub>4</sub> units)	57, 65
7	theoretical calculation (assumes WO <sub>3</sub> crystal structure)	37–39
4.5 <sup>a</sup>	CO chemisorption + FT-IR	36
4.7	CO chemisorption + FT-IR	64
4.5	Raman spectroscopy	42–44
6.2	XRD	62
~4.5 (model)	XPS	44
~5 (active)	XPS	44
~8	UV-vis DRS	38
4.1	H <sub>2</sub> reduction	38
~4.5	CO <sub>2</sub> chemisorption + FT-IR	38, 39, 63

<sup>a</sup>Converted from WO<sub>3</sub> mass fraction using specific surface area data reported in the papers.

active components can coexist in the highly active catalysts.<sup>69</sup> Therefore, knowledge of the key catalytically active sites is essential for catalyst design and optimization.<sup>70–75</sup> A general approach in the identification of catalytically active sites is to perform structural and chemical characterization on a systematic set of catalysts displaying different activities and then to correlate the structural information with catalytic performance measurements. A variety of such characterization techniques and catalytic performance testing studies have been applied to the WO<sub>3</sub>/ZrO<sub>2</sub> solid acid catalyst system in an effort to correlate the catalyst structure with catalytic performance.<sup>37–40,44,46,55,56,76</sup> The reactions catalyzed by WO<sub>3</sub>/ZrO<sub>2</sub> catalysts reported in the literature include alcohol dehydration reactions<sup>40,41,43–45</sup> and several hydrocarbon, primarily alkane, isomerization reactions.<sup>36,37,39,46,57,77</sup> In general, it has been found that the catalytic performance is a function of the surface WO<sub>x</sub> density on the zirconia support, as shown in Figure 4, and a function of both surface WO<sub>x</sub> density and calcination temperature, as shown in Figure 5. The maximum acidity is associated with an intermediate surface WO<sub>x</sub> density, but the precise “optimal” intermediate WO<sub>x</sub> surface density varies slightly depending on the reaction examined. There is also a general consensus that the structure of the supported WO<sub>x</sub> species depends on the surface WO<sub>x</sub> density present on the ZrO<sub>2</sub> support.<sup>36,38,42,43</sup> A number of specific surface species have been proposed to exist in this catalyst system at various WO<sub>x</sub> loading levels, including isolated monotungstate and oligomeric polytungstate species, WO<sub>x</sub> clusters, and well-ordered WO<sub>3</sub> nanocrystals.<sup>36, 38,42–46, 78–80</sup> Most of these structures were determined from optical spectroscopy techniques, including FTIR, Raman, and UV-vis diffuse reflectance spectroscopy, and until recently,<sup>44–46,81</sup> very limited effort has been made to provide direct electron microscopy images of these various WO<sub>x</sub> structures.<sup>78–80</sup> The lack of direct imaging of the different surface WO<sub>x</sub> species at the atomic scale undoubtedly led to some controversy in the early literature regarding the detailed structural models for the WO<sub>x</sub> catalytically active sites. Note that size-selected (WO<sub>3</sub>)<sub>3</sub> clusters have also been reported in model systems as active species.<sup>82,83</sup> However, such (WO<sub>3</sub>)<sub>3</sub> clusters are only present for model surface science studies where (WO<sub>3</sub>)<sub>3</sub> was deposited on oxide

single crystals and are not present for supported  $\text{WO}_x/\text{ZrO}_2$  powdered catalysts prepared by impregnation and coprecipitation.

The leading proposed structural models for the nature of the catalytically active sites present in solid acid  $\text{WO}_3/\text{ZrO}_2$  catalysts will be reviewed below. More recent research results based on in situ optical spectroscopy and atomic-resolution electron microscopy studies will be emphasized at the end of this section in an effort to provide additional atomic level details about the  $\text{WO}_3/\text{ZrO}_2$  solid acid catalysts.

**2.3.1. UC Berkeley Model for Catalytically Active Sites.** One of the most thorough investigations of the structure-activity relationship for  $\text{WO}_3/\text{ZrO}_2$  solid acid catalysts has been conducted by UC Berkeley researchers, who correlated the acidic catalytic activity to the surface  $\text{WO}_x$  structures deduced from a variety of in situ characterization techniques (X-ray absorption near-edge spectroscopy (XANES), UV-vis diffuse reflectance spectroscopy (DRS), Raman spectroscopy, and chemical titration techniques).<sup>37-41,56,84</sup>

UV-vis DRS is commonly used to establish the cluster (or domain) size of surface oxide species via analysis of the optical band gap energy.<sup>36-38</sup> The optical absorption edge energy,  $E_g$ , is defined as the minimum energy required to excite an electron from the highest occupied molecular orbital (HOMO) to the lowest unoccupied molecular orbital (LUMO),<sup>38</sup> or equivalently from the valence band to the conduction band for semiconducting metal oxides. Analogous to the case of a particle in a box, where the energy level separation increases with the decreasing dimension of the box, the UV-vis DRS characterization method relies on an inverse relationship between the edge energy ( $E_g$ ) and the cluster size of a semiconductor or insulator particle.<sup>38,47,68,85</sup> The measured UV-vis edge energies ( $E_g$ ), therefore, can only be used to qualitatively compare the cluster sizes of the dominant species in the  $\text{WO}_3/\text{ZrO}_2$  catalysts, such that a lower  $E_g$  is indicative of a larger  $\text{WO}_x$  cluster size and, hence, a more delocalized electron density.<sup>36,38</sup>

By analyzing the UV-vis DRS  $E_g$  values as a function of  $\text{WO}_x$  surface density, it was observed<sup>38</sup> that  $E_g$  decreases with an increasing  $\text{WO}_x$  surface density, as shown in Figure 8. The decreasing  $E_g$  value suggests the formation of larger polytungstate domains at high  $\text{WO}_3$  loadings.<sup>38</sup> It was proposed that the leveling off of the  $E_g$  values at surface densities higher

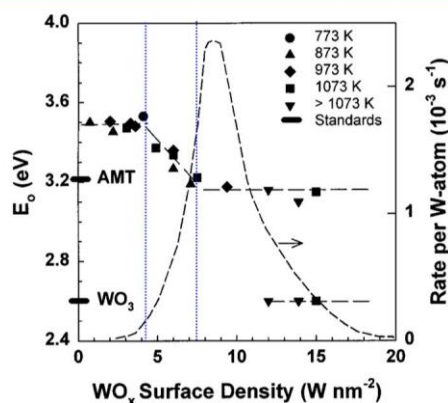


Figure 8. In situ UV-vis absorption edge energies as a function of surface  $\text{WO}_x$  density for a series of dehydrated  $\text{WO}_3/\text{ZrO}_2$  catalysts. The dashed curve shows the *o*-xylene isomerization rates per W atom on this particular set of catalysts. Adapted from ref 38.

than  $8 \text{ W/nm}^2$  was an indication of reaching monolayer coverage, which was consistent with the onset of crystalline  $\text{WO}_3$  formation, as detected by Raman spectroscopy and X-ray diffraction measurements on the same set of catalyst samples.<sup>38</sup>

Three distinct regions exist in the  $E_g$  plot presented in Figure 8, which were assigned to (i) the submonolayer surface monotungstate region ( $0-4 \text{ W/nm}^2$ ), (ii) the surface polytungstate growth region ( $4-8 \text{ W/nm}^2$ ), and (iii) a surface polytungstate/3D  $\text{WO}_3$  crystal coexistence region ( $>8 \text{ W/nm}^2$ ), respectively.<sup>38</sup> It was further proposed that only isolated surface monotungstate species exist for a surface  $\text{WO}_x$  density below  $4 \text{ W/nm}^2$ , as revealed by the constant UV-vis edge energy in this region.<sup>38</sup> For intermediate surface  $\text{WO}_x$  densities ( $4-8 \text{ W/nm}^2$ ), two-dimensional surface polytungstate structures become dominant, and the increase of surface  $\text{WO}_x$  density in this region leads to a monotonic increase of the surface polytungstate domain size until the monolayer coverage is reached at  $8 \text{ W/nm}^2$ . The

constant  $E_g$  value measured above  $8 \text{ W/nm}^2$  was attributed to the presence of 3D crystalline  $\text{WO}_3$  NPs.<sup>36</sup>

Corresponding in situ XANES experiments on the dehydrated  $\text{WO}_3/\text{ZrO}_2$  catalysts over a wide range of surface  $\text{WO}_x$  densities ( $3-15 \text{ W/nm}^2$ ) were also conducted. It was concluded from the XANES results that the  $\text{W}^{6+}$  centers in the surface  $\text{WO}_x$  species are present as distorted-octahedral  $\text{WO}_6$  units across the entire range of surface  $\text{WO}_x$  density.<sup>37,38</sup> The  $\text{W}^{6+}$  centers in the surface  $\text{WO}_x$  species are reducible and were proposed to be responsible for forming Brønsted acid sites ( $\text{H}^{\delta+}(\text{WO}_3)_n^{\delta-}$ ) during the acidic catalytic reactions.<sup>40,41</sup> The pre-edge region (1.5–3.2 eV) of the in situ UV-vis absorption spectra was used to monitor the reducibility of  $\text{WO}_x$  domains during acidic catalytic reactions,<sup>40,41</sup> and it was concluded that the maximum density for the reduced  $\text{WO}_x$  species occurred for intermediate surface  $\text{WO}_x$  densities. From a comparison of the proposed structures of the surface  $\text{WO}_x$  species and the catalytic activity as a function of surface  $\text{WO}_x$  density, it was concluded that the partially reduced surface polytungstate network structure provides an optimum compromise between  $\text{WO}_x$  reducibility and W atom accessibility, which comprises the physical state exhibiting the greatest number of catalytically active sites in the  $\text{WO}_3/\text{ZrO}_2$  catalyst system.<sup>37-41</sup>

The Berkeley interpretation of the surface  $\text{WO}_x$  species on  $\text{ZrO}_2$  as a function of surface  $\text{WO}_x$  density is depicted in Figure 9.

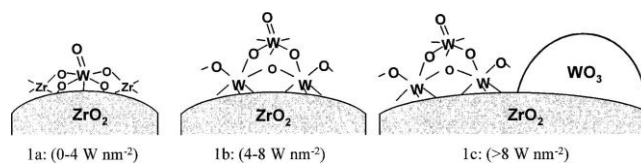


Figure 9. Structural models for the supported  $\text{WO}_x$  species present on the  $\text{ZrO}_2$  surface, as proposed by UC Berkeley researchers. Adapted from ref 38.

Two different approaches were employed to estimate the number of active sites, focusing on Brønsted acid sites. Using  $\text{NH}_3$ -IR spectroscopy combined with temperature-programmed desorption (TPD) measurements,<sup>39</sup> a ratio of 5 W atoms per Brønsted site was found at a surface density of  $5.5 \text{ W/nm}^2$ . From in situ pyridine and 2,6-di-*tert*-butylpyridine titration during 2-butanol dehydration,<sup>40</sup> however, a ratio of 25 W atoms per Brønsted site at a surface density of  $6.0 \text{ W/nm}^2$  was

reported, assuming that pyridine and 2,6-di-tert-butylpyridine block only one Brønsted acid site for 2-butanol dehydration. The discrepancy between the two methods was attributed to differences in the acidic strength, steric hindrance of the 2,6-di-tert-butylpyridine, and the competitive chemisorption mechanism between 2-butanol dehydration and the pyridines during these in situ titration studies. In accordance with the TOF calculation described in section 2.1.3, these two methods suggest that the catalytically active sites (considered to be Brønsted acid sites) represented only a minor fraction of the supported tungsten oxide.

Although not explicitly stated in the Berkeley papers, the increasing surface polytungstate domain size was correlated with the increasing catalytic activity in the 4–8 W/nm<sup>2</sup> surface density region.<sup>37,38</sup> Both “poly-tungstate” and “WO<sub>x</sub> clusters” terminologies were interchangeably used to describe the catalytically active site in the 4–8 W/nm<sup>2</sup> surface density region.<sup>37,38</sup> Monolayer surface coverages were reported to correspond to 8 W/nm<sup>2</sup>, which implies that the catalytically active site has a two-dimensional character (as indicated in the schematic in Figure 9). It was also proposed that strong acid sites can be generated by the replacement of a high-valent cation with ones of lower valence (e.g., W<sup>6+</sup> → (H<sup>δ+</sup>(WO<sub>3</sub>)<sub>n</sub><sup>δ-</sup>)). Monolayer surface coverage of WO<sub>x</sub> on ZrO<sub>2</sub> actually corresponds to ~4–5 W/nm<sup>2</sup>, as reviewed in section 2.2 and similarly suggested by CO<sub>2</sub> chemisorption (~4.5 W/nm<sup>2</sup>), UV-vis H<sub>2</sub> reduction (~4.1 W/nm<sup>2</sup>), and Raman spectroscopy (<5.0 W/nm<sup>2</sup>) measurements reported by the Berkeley group.<sup>39</sup> The proposed model is not consistent with the known monolayer surface WO<sub>x</sub> coverage on ZrO<sub>2</sub> of ~4.5–5.0 W/nm<sup>2</sup>.<sup>2,36,76,86</sup>

**2.3.2. University of München Model for Catalytically Active Sites.** The structural model for the catalytically active sites proposed by the University of München group and their co-workers emphasized an interesting effect related to the ZrO<sub>2</sub> support. In situ low-temperature IR spectroscopy coupled with CO adsorption was applied to the study of the surface cation species and their bonding with CO. The in situ IR spectra of the WO<sub>3</sub>/ZrO<sub>2</sub> catalyst prior to and after CO exposure are

shown in Figure 10. The IR bands of surface W O before CO chemisorption appear at 1024 and 1005 cm<sup>-1</sup> and were assigned to two independent surface W O species. Interestingly, low-temperature adsorption of CO on the surface of the WO<sub>3</sub>/ZrO<sub>2</sub> catalyst (estimated ~3.2 W/nm<sup>2</sup>) red-shifts the W<sup>3</sup>O IR<sup>2</sup> bands from 1024 to 1013 cm<sup>-1</sup> and from 1005 to 997 cm<sup>-1</sup>. It was proposed that this effect is caused by the inductive effect of CO coordinated to Zr<sup>4+</sup> sites in the vicinity of WO<sub>x</sub> species.<sup>36,76,86</sup> This red shift, however, was not observed in samples with high tungsten oxide loading above monolayer coverage, as Zr<sup>4+</sup> sites are no longer accessible by CO and could no longer affect the W O stretching bands.<sup>36,76,86</sup> It should be noted, however, that Zr<sup>4+</sup>-CO stretching bands were still observed in the IR spectra reported by the same group even when the tungsten oxide loading was much higher than monolayer coverage. This interesting experimental observation suggests that exposed Zr<sup>4+</sup> cations are still present in the catalyst above monolayer surface WO<sub>x</sub> coverage.

The University of München researchers proposed that the surface WO<sub>x</sub> network structure resembles pseudo-heteropolytungstates containing Zr<sup>4+</sup> cations (such a structure would have Zr<sup>4+</sup> in the center of a spherical cage where the cage wall is made up of mono-oxo WO<sub>6</sub> units). On correlation of this

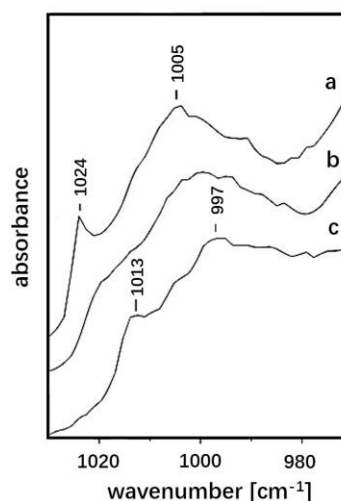


Figure 10. Low-temperature in situ IR spectra of a dehydrated 3.6% WO<sub>3</sub>/ZrO<sub>2</sub> (~3.2 W/nm<sup>2</sup>) 1098 K sample at 85 K showing the red shift of the W O stretching bands under CO adsorption at equilibrium pressures of (a) 0 mbar, (b) 0.1 mbar, and (c) 40 mbar. Adapted from ref 36.

observation with the acidity change in a systematic set of catalysts, it was proposed that a fully oxidized polytungstate WO<sub>x</sub> network incorporating trace levels of surface-exposed Zr<sup>4+</sup> and charge-compensating protons should be the catalytically active sites in the WO<sub>3</sub>/ZrO<sub>2</sub> catalyst system.<sup>36,76,86</sup> This model, however, does not account for the observed Zr<sup>4+</sup>-CO vibrations above monolayer coverage. Raman bands for such heteropolytungstate clusters of (XW<sub>12</sub>O<sub>40</sub>)<sup>3-</sup> are well documented<sup>87,88</sup> but have never been detected by any research group for supported WO<sub>3</sub>/ZrO<sub>2</sub> catalysts. Furthermore, silicotungstic acid (SiW<sub>12</sub>O<sub>40</sub>)<sup>3-</sup> supported on ZrO<sub>2</sub> thermally decomposes at 723 K, which is significantly below the calcination temperatures required to activate WO<sub>3</sub>/ZrO<sub>2</sub> catalysts (~923–1173 K) and, thus, cannot be present in activated WO<sub>3</sub>/ZrO<sub>2</sub> catalysts.<sup>47</sup> This model, therefore, also does not account for all of the reported observations about WO<sub>3</sub>/ZrO<sub>2</sub> catalysts.

**2.3.3. Mobil Model for Catalytically Active Sites.** A team of Mobil investigators focused on the chemical nature of the catalytically active sites present in the WO<sub>3</sub>/ZrO<sub>2</sub> catalyst system. Using a novel approach that combined XPS surface analysis and chemical titration with 2,6-dimethylpyridine and pyridine, the Mobil researchers<sup>57,77,89</sup> were able to quantify the population and strength of both surface Brønsted acid and Lewis acid sites in the catalysts. By correlating the catalytic performance and the concentration of strong surface Brønsted and Lewis acid sites, the Mobil group<sup>57,77,89</sup> postulated that a conjugate site having a 1:1 ratio of strong surface Brønsted to Lewis acid character would generate optimum catalytic performance for alkane isomerization, but a model for the molecular structure for such supported WO<sub>x</sub> catalytically active sites was not given.

The Mobil team also found that ~16 wt % W loading was required to maximize the acid site density of the catalyst, which they proposed represents coverage of about two mono-layers.<sup>57,77</sup>

However, it should be noted that the monolayer coverage used here is calculated by assuming WO<sub>4</sub><sup>2-</sup> monotungstates anchored to the ZrO<sub>2</sub> surface, i.e. ~3.6 W/nm<sup>2</sup>,<sup>57</sup> as discussed in section 2.2. The results thus suggest that

the Brønsted to Lewis acid ratio increases with surface  $\text{WO}_x$  density and peaks above  $4.5 \text{ W/nm}^2$  (typically  $6\text{--}7 \text{ W/nm}^2$ ), which is consistent with the formation of  $\text{Zr}\text{--}\text{WO}_x$  clusters above monolayer coverage.<sup>44–46,90</sup>

2.3.4. Lehigh–Rice–Virginia Model for Catalytically Active Sites. The work of the three aforementioned catalyst research groups provided many insights into the fundamental structure–activity relationship for the supported  $\text{WO}_3/\text{ZrO}_2$  catalysts, but the proposed models could not account for all the experimental observations and lacked direct supporting evidence.

The Lehigh–Rice–Virginia research group applied a wide range of characterization methods (including XRD, XPS, in situ Raman spectroscopy, in situ UV–vis DRS, and atomic resolution electron microscopy imaging) to carefully and systematically investigate two series of  $\text{WO}_3/\text{ZrO}_2$  catalyst systems side by side: namely, the highly active  $\text{WZrOH}$  catalysts (employing an amorphous  $\text{ZrO}_x(\text{OH})_{4-2x}$  support precursor) and low-activity model  $\text{WZrO}_2$  catalysts (using a crystalline  $\text{ZrO}_2$  (monoclinic) support).<sup>42–46,49</sup> While Raman and UV–vis spectroscopy provide local structure and electronic information at the molecular level from sampling volumes of  $\sim 100 \text{ nm}$ , electron microscopy can provide detailed structural and compositional information with atomic resolution at the nanometer scale to complement the optical spectroscopy studies.

The molecular structures of the different  $\text{WO}_x$  species present on  $\text{ZrO}_2$  supports were determined from combined in situ UV–vis and Raman spectroscopy. For the model supported  $\text{WO}_3/\text{ZrO}_2$  catalyst system, the  $E_g$  values derived from UV–vis DRS measurements as a function of surface W density are shown in Figure 11. Comparison of the  $E_g$  values for

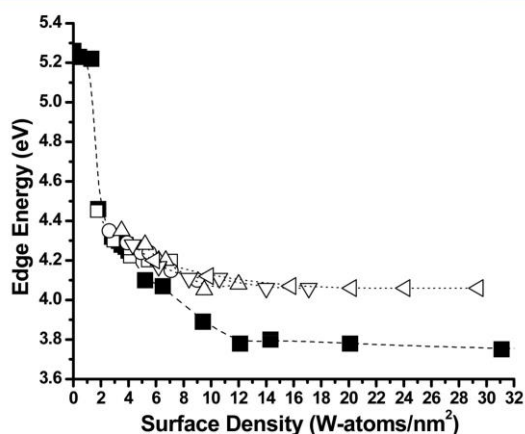


Figure 11. UV–vis DRS edge energy,  $E_g$  (eV), for supported tungsten oxide catalysts as a function of surface density ( $\text{W atoms/nm}^2$ ) for “model”  $\text{WZrO}_2$  catalysts ( $\blacksquare$ ) and highly active  $\text{WZrOH}$  catalysts calcined at different temperatures (open symbols). Adapted from ref 44.

the model  $\text{WO}_3/\text{ZrO}_2$  catalysts with  $\text{WO}_x$  reference compounds in Figure 12, reveals that isolated surface monotungstate species are only present below a tungsten oxide surface density of  $\sim 1 \text{ W/nm}^2$  ( $E_g \approx 5.2\text{--}5.3 \text{ eV}$ ) and that the surface  $\text{WO}_x$  species become progressively more polymerized as surface polytungstates as monolayer surface coverage of  $\sim 4.5 \text{ W/nm}^2$  is attained ( $E_g \approx 4.2 \text{ eV}$ ).<sup>43,44,47</sup> Above monolayer coverage ( $>4.5 \text{ W/nm}^2$ ), the UV–vis DRS  $E_g$  values drop further to  $\sim 3.8 \text{ eV}$  and approach the  $E_g$  value characteristic of bulk  $\text{WO}_3$  crystals, reflecting the dominance of the  $\text{WO}_3$  phase in these catalysts.

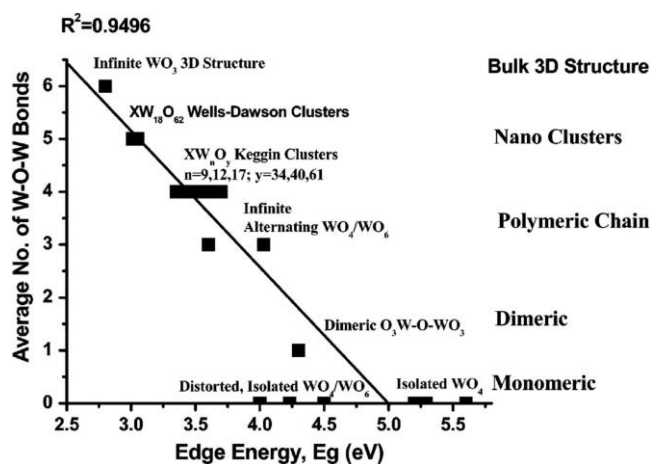


Figure 12. Correlation between the UV–vis DRS edge energy ( $E_g$ ) and the average number of bridging  $\text{W}\text{--}\text{O}\text{--}\text{W}$  bonds around the central  $\text{W}^{6+}$  cation in bulk tungstate reference compounds. Adapted from ref 47.

The corresponding in situ Raman spectra of the model  $\text{WZrO}_2$  are presented in Figure 13. The vibrations below  $700$

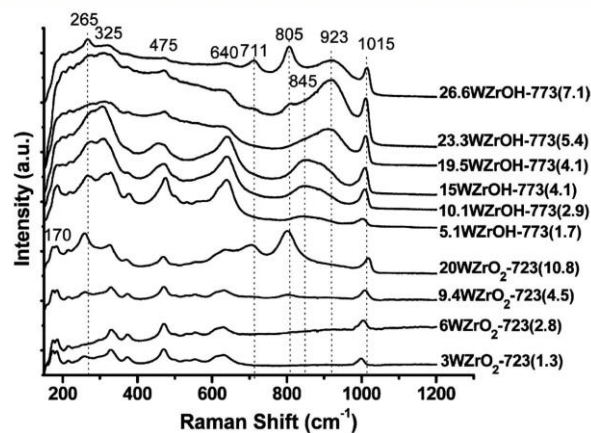


Figure 13. Comparison of in situ Raman spectra as a function of tungstate surface density for supported  $\text{WZrO}_2\text{-723}$  and  $\text{WZrOH-773}$  catalysts under dehydrated conditions. Adapted from ref 44.

$\text{cm}^{-1}$  arise from the  $\text{ZrO}_2$  (monoclinic) support, and the vibrations above  $700 \text{ cm}^{-1}$  are associated with the supported tungsten oxide phase. Up to monolayer surface coverage ( $4.5 \text{ W/nm}^2$ ), only one band is present at  $\sim 1000 \text{ cm}^{-1}$  characteristic of surface  $\text{WO}_x$  species on the  $\text{ZrO}_2$  support (i.e., mono-oxo

$\text{O WO}_4$  species). The continuous shift in the Raman band from  $\sim 990$  to  $1015 \text{ cm}^{-1}$  with increasing tungsten oxide coverage reflects the progressive polymerization of the surface  $\text{WO}_x$  species. Above monolayer coverage ( $>4.5 \text{ W/nm}^2$ ), new bands from crystalline  $\text{WO}_3$  nanoparticles are also present at  $805$  and  $715 \text{ cm}^{-1}$ , in agreement with the decreasing  $E_g$  trends obtained from UV–vis spectroscopy in Figure 11.

The UV–vis DRS  $E_g$  trend with surface W density for the active  $\text{WZrOH}$  catalysts is similar to that for the model  $\text{WZrO}_2$  catalysts, as shown in Figure 11, initially rapidly decreasing due to polymerization of the surface  $\text{WO}_x$  species and asymptotically stabilizing above monolayer coverage. However, the asymptotic  $E_g$  value is  $\sim 4.1 \text{ eV}$  vs  $3.8 \text{ eV}$  for the model catalyst, reflecting the smaller  $\text{WO}_x$  domains for the highly active catalyst. The corresponding Raman spectra are presented

in Figure 13. The major difference between the Raman spectra of the highly active WZrOH and the model WZrO<sub>2</sub> catalysts is the presence of the broad bands in the ~820–850 and ~900–925 cm<sup>-1</sup> ranges for the active WZrOH catalysts. These bands can plausibly arise from Zr-stabilized disordered WO<sub>3</sub> NPs, since crystalline WO<sub>3</sub> exhibits its highest vibration at 805 cm<sup>-1</sup> and structural distortions will shift this band to higher wavenumbers.<sup>44</sup> The broader bands at ~990–925 cm<sup>-1</sup> are related to highly disordered Zr-WO<sub>3</sub> NPs having a greater amount of zirconia present, and the sharper ~820–850 cm<sup>-1</sup> bands arise from mildly disordered Zr-WO<sub>3</sub> NPs containing a lower amount of zirconia. The comparative spectroscopic results reveal that the difference between the highly active WZrOH catalysts and less active WZrO<sub>2</sub> catalysts is the presence of distorted Zr-WO<sub>3</sub> NPs in the former.

Although in situ Raman and UV-vis spectroscopy provide molecular and electronic structural information about the different supported WO<sub>x</sub> species on ZrO<sub>2</sub>, these optical techniques cannot provide information on the spatial distribution of the various supported WO<sub>x</sub> phases with atomic resolution. In order to identify the detailed atomic structure of the surface supported species, atomic resolution electron microscopy studies on a systematic set of supported WO<sub>3</sub>/ZrO<sub>2</sub> catalysts having different surface tungstate loadings and catalytic activities were performed.<sup>44–46,90</sup> Conventional high-resolution transmission electron microscopy (HR-TEM) imaging, as commonly used to study the crystal structure of catalyst materials at the atomic scale,<sup>90</sup> was first performed on active supported WO<sub>3</sub>/ZrO<sub>2</sub> catalysts.<sup>44</sup> As shown in Figure 14,

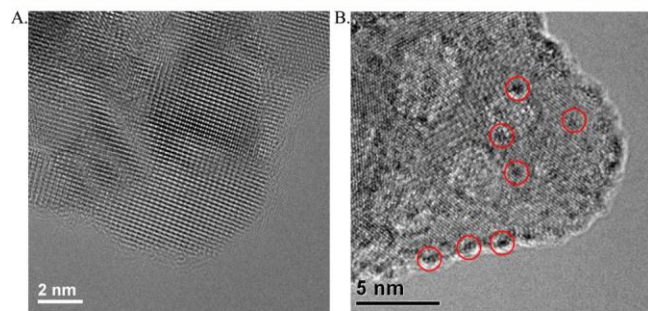


Figure 14. Representative HR-TEM images from (A) a WZrOH catalyst having a low catalytic activity (2.9WZrOH-773 K, with a surface WO<sub>x</sub> density of 2.9 W/nm<sup>2</sup> and calcination temperature of 773

K) and (B) a WZrOH catalyst having a high catalytic activity (6.2WZrOH-1073 K). Red circles denote WO<sub>x</sub> clusters with diameter ~0.8–1 nm. These latter clusters were only found in samples with surface W density above monolayer coverage, which exhibit higher catalytic performance.<sup>44,45</sup> Adapted from refs 44 and 45.

the lattice fringes from the ZrO<sub>2</sub> support particles can be well resolved and clusters ~1 nm in size can be clearly observed in samples having a surface W density exceeding monolayer coverage, as highlighted in Figure 14B. HR-TEM imaging, however, fails to provide any structural information about the surface isolated monotungstate and oligomerized polytungstate species (Figure 14A), as they display very little image contrast due to their highly dispersed nature and the underlying image formation mechanism of HR-TEM.<sup>90</sup>

When high-angle annular dark-field (HAADF) imaging in an aberration corrected STEM is used, which provides atomic number (Z) contrast, direct imaging of all the surface WO<sub>x</sub> entities on the ZrO<sub>2</sub> support at all surface WO<sub>x</sub> density loadings

becomes possible.<sup>45</sup> The STEM-HAADF imaging results from a systematic set of supported WZrOH catalysts having different surface tungstate loadings and catalytic activities are summarized in Figure 15. In this imaging mode, individual heavy atoms

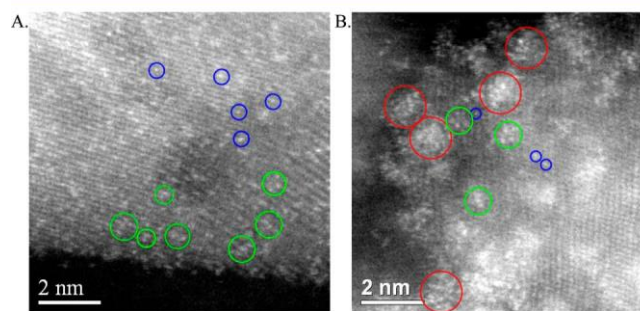


Figure 15. Representative STEM-HAADF images of supported WZrOH<sub>2</sub> catalysts: (A) a less active catalyst with low WO<sub>x</sub> surface density; (B) a highly active catalyst with surface density higher than the monolayer coverage. The blue circles highlight the presence of single W atoms corresponding to isolated surface monotungstate species, and the green circles indicate oligomeric surface polytungstate species with several W atoms linked by oxygen bridging bonds. The red circles highlight Zr-WO<sub>x</sub> mixed oxide clusters with diameter ~0.8–1 nm. These last clusters are only found in the highly active catalyst samples having a surface WO<sub>x</sub> density above monolayer coverage and are identified as the most reactive catalytically active species. Adapted from ref 45.

appear as bright spots, and the atoms with larger atomic number, i.e. W in this case, display higher image contrast against the ZrO<sub>2</sub> support particles. For the low-activity sample with surface density below the monolayer coverage, the WO<sub>x</sub> was found to be highly dispersed on the ZrO<sub>2</sub> surface mainly as mono- and polytungstate species with single atomic layer thickness (Figure 15A). The existence of the surface WO<sub>x</sub> species has long been proposed in the literature from Raman spectroscopy, but this work represented the first time that they had been directly imaged. The high-activity samples with surface density above monolayer coverage, however, possess additional numerous disordered WO<sub>x</sub> clusters ~0.8–1.0 nm in size (Figure 15B) coexisting with the surface mono- and polytungstate species. Determining the composition of such small clusters would be almost impossible using other techniques; however, the Z-contrast images also contain such useful information. By careful analysis of the subtle contrast variation observed in HAADF images from these ~1 nm clusters, it was proposed that they were in fact mixed oxide clusters containing both Zr cations and WO<sub>x</sub> species,<sup>44–46</sup> an assertion which was supported by results from in situ Raman spectroscopy studies,<sup>44</sup> novel catalyst design experiments,<sup>45</sup> and image simulations.<sup>45,46,49</sup>

The catalytic activities of the supported tungstated zirconia catalysts were investigated for both methanol dehydration<sup>44,45</sup> and n-pentane isomerization<sup>46</sup> reactions, and a similar surface W density dependence of the catalytic activity was found for both reactions. Specifically, in the low surface WO<sub>x</sub> density region (<4.5 W/nm<sup>2</sup>), corresponding to the submonolayer coverage regime, the WO<sub>3</sub>/ZrO<sub>2</sub> materials display low catalytic activity, while high activity was observed for catalysts with surface WO<sub>x</sub> densities higher than 4.5 W/nm<sup>2</sup>, corresponding to a surface coverage exceeding a monolayer. The complementary structural/activity information provided by these different characterization techniques provides an in-depth

overview of the  $\text{WO}_3/\text{ZrO}_2$  structures from the macro scale down to the single-atom level, which can be correlated with the catalytic performance data.

The ability to visualize all of the supported tungstate species present in a systematic set of samples displaying a variety of catalytic activities allowed the Lehigh-Rice-Virginia group to draw a direct correlation between the supported tungstate structures and their catalytic performance. By combining structural information from aberration corrected STEM-HAADF imaging studies and complementary in situ Raman, UV-vis spectroscopy data, it was shown that surface isolated monotungstate and oligomeric polytungstate species are the dominant  $\text{WO}_x$  entities on the  $\text{ZrO}_2$  surface when the surface density is lower than monolayer coverage ( $\sim 4.5 \text{ W/nm}^2$ ) and that additional disordered mixed oxide Zr- $\text{WO}_x$  clusters  $\sim 0.8\text{--}1.0 \text{ nm}$  in size coexist with the surface mono- and polytungstate species once the surface W density exceeds monolayer coverage,<sup>44,45</sup> as shown schematically in Figure 16. The use

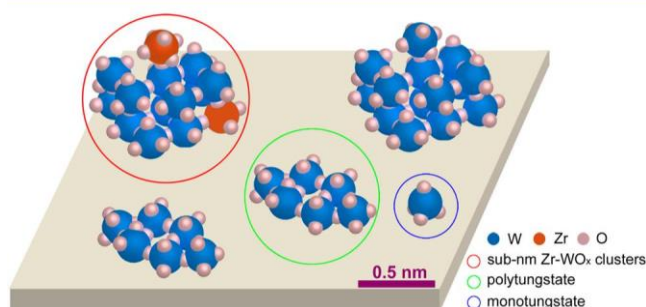


Figure 16. Schematic representation of isolated surface monotungstate (blue circle), oligomeric two-dimensional polytungstate (green circle), and three-dimensional Zr- $\text{WO}_3$  clusters (red circle) and crystalline  $\text{WO}_3$  NPs (no circle) supported on  $\text{ZrO}_2$  surfaces. Adapted from ref 90.

of an amorphous  $\text{ZrO}_x(\text{OH})_{4-2x}$  support precursor provides easy access to surface Zr cations that can be extracted and incorporated into the  $\text{WO}_x$  clusters during crystallization by calcination above the Hüttig temperature of  $\text{ZrO}_2$  (where surface species have sufficient mobility to agglomerate and sinter) and help to generate the highly active mixed Zr- $\text{WO}_x$  cluster sites.<sup>45</sup> A further increase in tungsten oxide loading results in the formation of inactive bulk  $\text{WO}_3$  crystals. By correlation of the structural information with catalytic performance, it was possible to conclude that the least active sites are the isolated surface monotungstate species ( $\sim 1 \text{ W/nm}^2$ ) and the surface polytungstate species are only slightly more active ( $\sim 1.5\text{--}4.5 \text{ W/nm}^2$ ), as reflected by their respective catalytic activity (see Figures 5 and 6). The well-ordered  $\text{WO}_3$  nanoparticles present in the model  $\text{WZrO}_2$  catalysts are slightly more active than the surface tungstate species (see Figures 5 and 6). The  $\sim 1 \text{ nm}$  disordered Zr- $\text{WO}_x$  mixed oxide clusters only present in the supported  $\text{WZrOH}$  catalyst system, however, are unequivocally the most active catalytic sites for both the methanol dehydration and n-pentane isomerization reactions.<sup>44-46</sup> This model accounts for all the reported experimental observations and the presence of exposed  $\text{Zr}^{4+}$  sites above monolayer surface coverage.

**2.3.5. Theoretical Insights into the Acidity of  $\text{WO}_x/\text{ZrO}_x$  Domain Structures.** The catalytic activity of solid acid catalysts is often linked to the acidity of the catalyst.<sup>91-101</sup> Much can be learned about the reactivity of solid acid catalysts by

understanding their intrinsic acidity, provided that the solvation environment remains the same and there are minimal confinement effects.<sup>102,103</sup> While the adsorption of basic probe molecules and in situ spectroscopy provide insights into structural and electronic features that influence acidity, there are no direct experimental probes of solid acidity.<sup>91</sup> Ab initio simulations of the deprotonation energy (DPE), which is the energy required to remove a proton from the solid acid to form the conjugate base and a separated proton, can provide an idealized yet direct measure of the Brønsted acidity. Such simulations have helped to provide establish the intrinsic acidity for a wide range of model solid acids, including zeolites<sup>92,93</sup> and heteropolyacids.<sup>94-100</sup> The results for many of these systems have shown direct correlations between the rate constants for solid acid catalyzed reactions and the deprotonation energies of the acid for different reactions, including dehydration and isomerization, provided that the entropic changes for such systems are small. Macht et al.<sup>99</sup> extended the direct linear relationship between the logarithm of experimentally measured intrinsic rate constants and theoretically calculated DPE values for heteropolyacids. They used experimentally measured rate constants for the dehydration and isomerization to regress or back-calculate DPE values for sulfated zirconia (1110 kJ/mol (isomerization) and 1120 kJ/mol (dehydration)) as well as tungstate zirconia (1120 kJ/mol (isomerization) and 1185 kJ/mol (dehydration)) for isomerization and dehydration reactions.

The acidic properties of the different model domain structures present on supported  $\text{WO}_x/\text{ZrO}_x$  catalysts discussed herein were calculated using density functional theory (DFT). The model domain structures chosen for investigation consisted of single-layer 2D  $\text{WO}_x$  structures (isolated  $\text{WO}_x$ ,  $\text{W}_2\text{O}_x$  dimers, and  $\text{W}_y\text{O}_x$  oligomers) on  $\text{ZrO}_2$ , which are shown in Figure 17, and three-dimensional Zr-promoted  $\text{WO}_x$  clusters

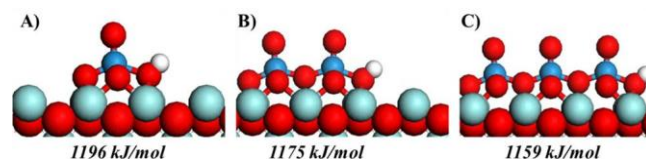


Figure 17. Structures and deprotonation energies of model (a) monomeric  $\text{WO}_4$ , (b) dimeric  $\text{W}_2\text{O}_7$ , and (c) trimeric  $\text{W}_3\text{O}_{10}$  clusters supported on  $\text{ZrO}_2$ . The tungsten, zirconium, oxygen, and hydrogen atoms are shown in blue, light blue, red, and white, respectively.

( $\text{ZrO}_x$  containing polyoxotungstate Keggin structures with monomeric  $\text{ZrO}_x$  in different locations), shown in Figure 18, that were chosen to mimic the active sites.

While the specific atomic structures of the active sites in the Zr- $\text{WO}_x$  systems are still unclear, the detailed STEM-HAADF imaging, in situ Raman and UV-vis spectroscopy, and kinetic studies discussed in section 2.3.4 indicate that the active environments are comprised of structurally distorted and disordered three-dimensional Zr- $\text{WO}_x$  clusters on the order of  $0.8\text{--}1 \text{ nm}$  in size where the W resides in distorted-octahedral environments in direct contact with exposed Zr cations. In order to provide a more direct understanding of the influence of structure on reactivity, we carried out calculations on well-defined model 3D Zr- $\text{WO}_x$  systems. The  $\text{ZrO}_x$ -supported and Zr-substituted tungstate Keggin structures presented in Figure 18 match many of the structural attributes of the active Zr- $\text{WO}_x$  clusters presented in section 2.3.4 in that they are  $\sim 1 \text{ nm}$

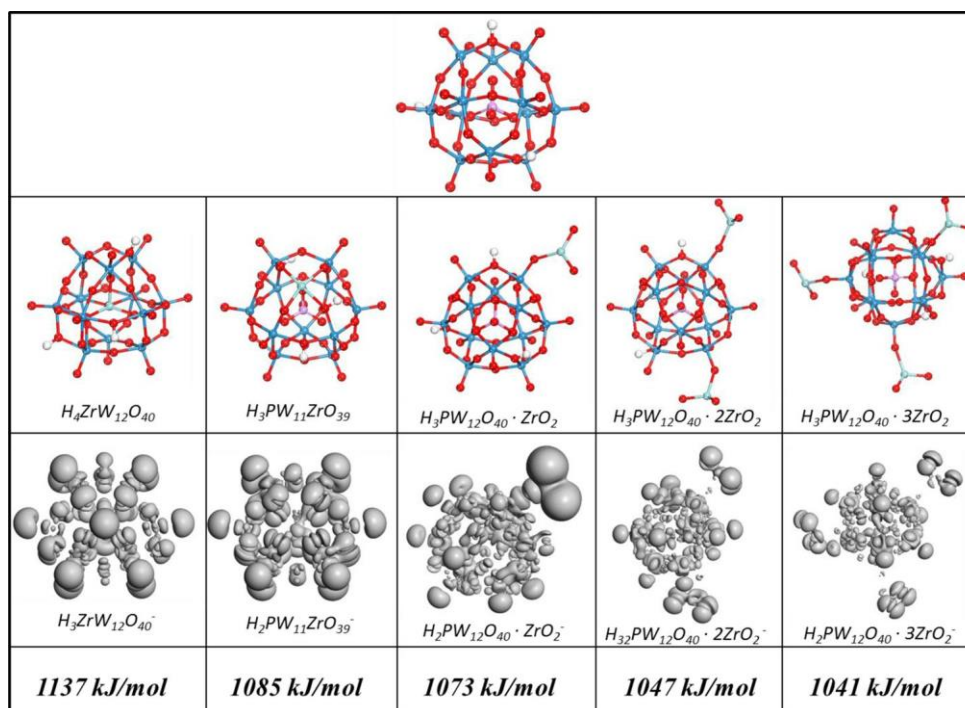


Figure 18. Deprotonation energies (DPE) and electron density difference maps for the conjugate bases of model  $ZrO_x$ -containing polytungstate Keggin clusters. The structures examined include  $ZrO_4^{4-}$  in the central shell ( $H_4ZrW_{12}O_{40}$ ),  $ZrO_4$  in the outer addenda shell ( $H_3PW_{11}ZrO_{39}$ ), and one, two, and three attached  $ZrO_2$  clusters. Color scheme: red, O; blue, W; purple, P; cyan, Zr; white, H.

diameter  $WO_x$  clusters in distorted-octahedral environments and in direct contact with Zr cations. While these models provide a reasonable local structure, they are overly simplified models. At the higher temperatures of reaction, the Keggin structures are known to undergo cage opening and structural rearrangements. While such structural reorganization would change the environment, the local distorted Zr- $WO_x$  architecture would still likely maintain the distorted Zr- $WO_x$  clusters with similar structure.

The Keggin models used examine Zr substituted at addenda sites as well as  $ZrO_x$  clusters anchored to the exterior of the  $H_3PW_{12}O_{40}$  cluster. These models capture the  $Zr^{4+}$ -CO vibrational stretches that are observed experimentally at greater than monolayer  $WO_x$  coverages, thus overcoming one of the issues of the Munich model which assumed that the  $ZrO_x$  is encapsulated in the interior of the  $WO_x$  outer shell. The Keggin models used here, however, are still very simplified models of the active sites.

For the 2D  $WO_x$  structures supported on  $ZrO_2$  (shown in Figure 17), there is a significant increase in acidity and activity of Zr-O(H)-W Brønsted acid sites as the  $WO_x$  domain size increases from monomers (1196–1203 kJ/mol) to dimers (1175–1185 kJ/mol) to oligomers (1090–1180 kJ/mol). This is consistent with recent in situ  $^1H$  NMR and  $^{13}C$ -acetone adsorption experiments and theoretical simulations which indicate that the dimeric W-OH-Zr sites are much more acidic than the monomeric W-OH sites.<sup>101</sup> The increase in acidity with an increase in the  $WO_x$  domain size is directly associated with the ability of the conjugate base that results upon deprotonation of the acid to delocalize electrons. The acidity and activity of Zr-O(H)-W sites in the 3D structures, however, are significantly higher than those of any of the 2D structures. The DPE values calculated here for the  $ZrO_2$ -supported polytungstates which range from 1090 to 1185 kJ/

mol are consistent with the values of 1120–1185 kJ/mol that were back-calculated from experimental dehydration and isomerization kinetics by Macht et al.<sup>99</sup>

To better understand the variation of acidity and activity of the 3D  $ZrO_x$ - $WO_x$  structures as a function of the location of  $ZrO_x$ , the Zr-substituted or Zr-promoted  $H_3PW_{12}O_{40}$  Keggin structures discussed above were used. To examine the effect of  $ZrO_x$  on the acidity and activity of the 3D  $H_3PW_{12}O_{40}$  polytungstate cluster,  $ZrO_x$  was placed in different positions by (a) substituting Zr for W addenda atoms, (b) substituting Zr for the central P atom, and (c) supporting model  $ZrO_x$  clusters on the  $H_3PW_{12}O_{40}$  cluster, as shown in Figure 18.

The deprotonation energies for the 3D Keggin Zr- $WO_x$  clusters shown in Figure 18, with the exception of the  $H_4ZrW_{12}O_{40}$  structure, where Zr acts as the central cation Keggin unit, were all calculated to be 70 kJ/mol lower and hence more acidic than the 2D polymeric  $WO_x/ZrO_2$  structures. The increase in the DPE value (to 1137 kJ/mol) for the  $H_4ZrW_{12}O_{40}$  structure is due to the increased number of charge-balancing protons from 3 to 4, which decreases the Keggin acidity as it decreases the strength of the conjugate base, as the Keggin structure less readily delocalizes the excess negative charge. The lowest DPE values (1073–1041 kJ/mol) and hence highest Brønsted acid site strengths were found for  $ZrO_x$  clusters supported on the external surface of the  $H_3PW_{12}O_{40}$  cluster with calculated DPE values decreasing with increasing numbers of  $ZrO_2$  and  $ZrO_4^{4-}$  clusters bound to the external surface. The charge density difference maps plotted in Figure 18 indicate that the supported zirconia cluster(s) on the Keggin structure can more easily delocalize the electron density over the polytungstate structure, which in turn increases its Brønsted acidity. The increase in the number of  $ZrO_x$  clusters further increases the delocalization and stabilization of the polytungstate Keggin cluster.

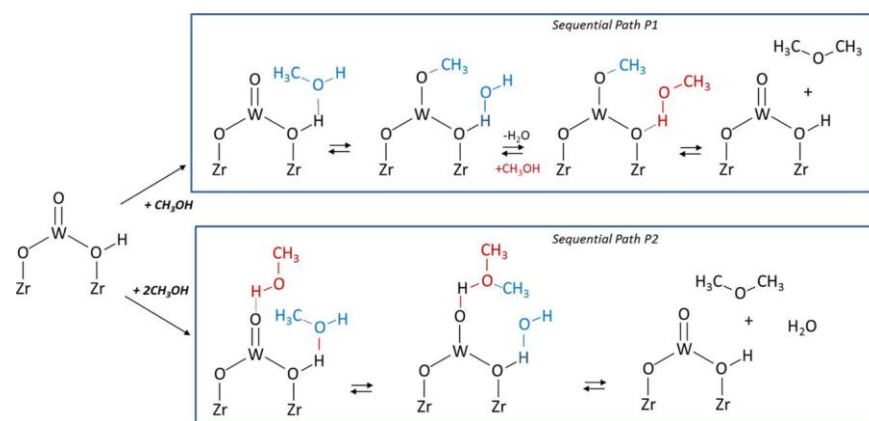


Figure 19. Sequential (P1) and simultaneous (P2) methanol dehydration pathways over tungstated zirconia.

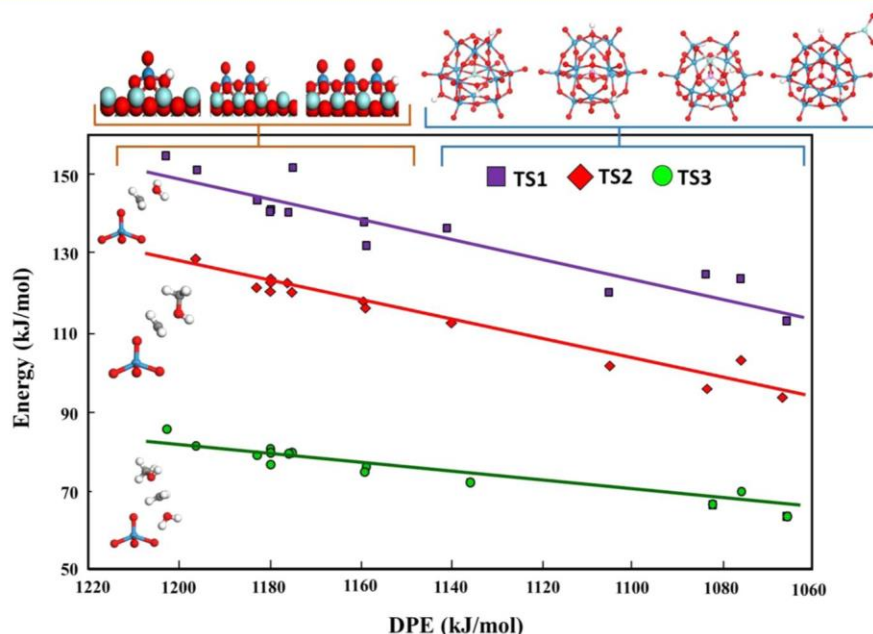


Figure 20. Activation barriers for both the sequential and simultaneous methanol dehydration paths plotted against deprotonation energies of the acid sites on tungstated zirconia. TS1, TS2, and TS3 refer to the transition states for the H<sub>2</sub>O elimination step in the sequential path, the DME formation step in the sequential path, and direct DME formation in the simultaneous path, respectively. The 3D Keggin-type Zr-WO<sub>x</sub> structures are more acidic and more reactive than the 2D WO<sub>x</sub>/ZrO<sub>2</sub> structures and, as such, lie to the right-hand side.

**2.3.6. Theoretical Aspects of Acidity–Activity Relationships for Tungstated Zirconia.** Methanol dehydration was used as a chemical probe reaction to study the acidity–activity relationship in the 2D and 3D tungstated zirconia systems.<sup>42,45</sup> There are two different pathways by which the reaction can proceed.<sup>95–100</sup> The first proceeds by the sequential activation of methanol to form a methoxy intermediate and a water molecule. This is followed by the adsorption of a second methanol molecule and its reaction with the adsorbed methoxy to form dimethyl ether and regenerate the acid site. The second path proceeds by the simultaneous addition of the two adsorbed methanol molecules to form DME and water, which desorb from the surface. The simultaneous path avoids forming the strongly bound methoxy intermediate. The elimination of water is calculated to be the rate-limiting step for both of these paths. These methanol reaction pathways are shown in Figure 19.

The activation barriers for the rate-limiting elimination step in methanol dehydration for both mechanisms have been

calculated for all 2D surface tungstate domains and various 3D tungstate-zirconia mixed oxide Keggin clusters and are plotted against the DPEs in Figure 20. In general, the Brønsted acidity increases as the tungstate domain size increases. The increased acidity subsequently results in lower activation barriers and higher reactivity.

The supported WO<sub>x</sub>/ZrO<sub>2</sub> results all lie on the left-hand side of Figure 20, where the DPE values decrease from 1196 to 1100 kJ/mol on moving from the monomeric to polymeric WO<sub>x</sub>/ZrO<sub>2</sub> structures. The activation barriers for the methoxy formation transition state (TS1) and the DME formation transition state (TS2) involved in the sequential dehydration path and the transition state for the direct simultaneous path (TS3) decrease from 151 to 138 kJ/mol, from 129 to 118 kJ/mol, and from 81 to 75 kJ/mol, respectively, with increasing acidity.

The 3D Zr-WO<sub>x</sub> Keggin structures, as discussed above, are much more acidic and, as such, they lie along the right-hand side of Figure 20 with DPE values that range from 1089 to

1060 kJ/mol. The barriers for TS1, TS2, and TS3 were calculated to be respectively 6–8, 22–23, and 20–30 kJ/mol lower than those for the polymeric  $\text{WO}_x$  clusters on  $\text{ZrO}_2$ . Despite the differences in structure between the 2D  $\text{WO}_x/\text{ZrO}_2$  and 3D  $\text{Zr-WO}_x$  Keggin structures, they follow the same linear relationships between acidity and activity as shown in Figure 20. This is consistent with the reactions carried out on other

solid acids such as sulfated zirconia,<sup>99</sup> heteropolyacids,<sup>94,96,97,99,100</sup> and zeolites,<sup>92,93,104</sup> which provide the ranking

zeolites < perfluoro- sulfonic resins <  $\text{WO}_x/\text{ZrO}_2$

< sulfated zirconia < W-heteropolyacids

When the slopes of three acidity–activity trend lines in Figure 20 are compared, it is clear that the dehydration activation barriers in the sequential paths are much more sensitive to changes in catalyst acidity than the steps involved in the simultaneous pathway. The acidity–activity sensitivity is largely dependent on the structure of the transition state or, more specifically, on how the carbenium ion is stabilized in the transition state. One can see in Figure 20 that the methyl carbenium ions that form in the sequential path transition states are directly stabilized by the surface oxygen atom on the Keggin structure as well as by the water that is eliminated in the first reaction step or by the coadsorbed methanol in the second reaction step. The methyl carbenium ion in the simultaneous path transition state, however, is stabilized by the coreactant methanol molecule and the eliminated water as well as by the oxygen on the Keggin structure. The extra water or methanol molecule in this latter path significantly stabilizes the transition state, as is shown by the lower energy barriers. In addition, it further removes the methyl carbenium ion from the negatively charged  $\text{O}^*$  on the Keggin structure. The addition of the extra water and the change in the structure both act to significantly lower the sensitivity of the reaction to acid site strength.

The results from the DFT calculations are in full agreement with the experimental findings that the most active Brønsted acid sites in the supported  $\text{WO}_x/\text{ZrO}_2$  solid acid catalysts are associated with 3D mixed  $\text{Zr-W-O}$  clusters. The optimum size of the  $\text{Zr-W-O}$  clusters cannot be directly estimated by these calculations, but it is demonstrated experimentally to be in the 0.8–1 nm range.

### 3. CATALYST DESIGN AND OPTIMIZATION

The identification of ~1 nm mixed oxide  $\text{Zr-WO}_x$  clusters as the most reactive catalytically active site<sup>44–46</sup> provides a new perspective for solid acid supported oxide catalyst research and suggests new directions for the rational design of such catalysts with enhanced performance. This principle has been demonstrated by coimpregnating amorphous  $\text{ZrO}_x$  and  $\text{WO}_x$  precursors onto a crystalline  $\text{ZrO}_2$  support followed by high-temperature calcination to synthesize the  $\text{Zr-WO}_x$  clusters via thermally activated surface diffusion.<sup>45</sup> The catalyst design experiment made use of a relatively inactive model supported  $\text{WZrO}_2$  catalyst ( $2.5\text{WZrO}_2$ -723 K) that had below monolayer coverage as the starting material, which was postimpregnated with (i)  $\text{ZrO}_x$  or  $\text{WO}_x$  precursors separately or (ii) both precursors simultaneously, followed by a 973 K calcination step.

Simultaneous coimpregnation of both  $\text{WO}_x$  and  $\text{ZrO}_x$  precursors was designed to mimic the formation of mixed-oxide clusters on the  $\text{ZrO}_2$  surface during calcination. The 973 K calcination temperature was carefully chosen to be slightly higher than the 896 K Hüttig temperature of  $\text{ZrO}_2$  (at which

surface  $\text{ZrO}_2$  species have sufficient mobility to agglomerate and sinter) but well below the 1494 K Tammann temperature of  $\text{ZrO}_2$ . This intermediate temperature of 973 K would therefore promote the intermixing of the surface  $\text{WO}_x$  and  $\text{ZrO}_x$  species into the mixed oxide clusters without activating bulk diffusion of Zr species from the bulk  $\text{ZrO}_2$  crystal.

Aberration corrected STEM-HAADF imaging was employed to monitor the structural evolution of the surface  $\text{WO}_x$  species during the postimpregnation process. As shown in Figure 21A,

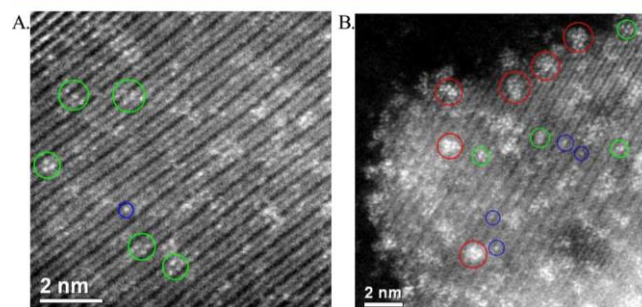


Figure 21. Aberration-corrected STEM-HAADF images of (A) the starting model  $\text{WZrO}_2$  catalyst ( $2.5\text{WZrO}_2$ -723 K) and (B) the  $\text{ZrO}_x$  and  $\text{WO}_x$  postimpregnated catalyst ( $(3.5\text{W}+3.5\text{Zr})/2.5\text{WZrO}_2$ -973 K). Adapted from ref 45.

the starting low-activity  $2.5\text{WZrO}_2$ -723 K model catalyst exclusively shows highly dispersed surface monotungstate and polytungstate species, as expected. The simultaneously  $\text{ZrO}_x$  and  $\text{WO}_x$  postimpregnated sample shows an additional high-density population of subnanometer mixed oxide clusters, containing both W and Zr cations, as evidenced by subtle contrast variations within single clusters (Figure 21B).

The formation of mixed oxide clusters in the coimpregnated catalyst was found to dramatically increase the catalytic activity for the methanol dehydration reaction by more than 2 orders of magnitude relative to the starting model catalyst. In contrast, postimpregnation with the  $\text{ZrO}_x$  precursor or the  $\text{WO}_x$  precursor alone gave only a minimal improvement in catalytic performance.<sup>45</sup> These results provide strong complementary support for the catalytically active site structural model that three-dimensional 0.8–1.0 nm mixed  $\text{Zr-WO}_x$  clusters constitute the most reactive catalytically active species in the  $\text{WZrOH}$  catalyst system.<sup>45</sup>

Some other important contributions toward the development of monodisperse  $\text{Zr-WO}_x$  supported catalysts have also been made very recently. Song et al.<sup>28</sup> synthesized a novel  $\text{WO}_3/\text{ZrO}_2$  catalyst via a two-phase interface hydrolysis (TPIH) method. The catalysts demonstrated an enhanced n-pentane isomerization performance due to their thermostructural stability that resulted in higher amorphous  $\text{WO}_x$  loadings after calcination. The Raman spectra presented in their work clearly demonstrated that the most active TPIH  $\text{WO}_3/\text{ZrO}_2$  catalyst ( $6.0 \text{ W/nm}^2$ ) shows the highest concentration of highly distorted  $\text{Zr-WO}_x$  clusters, even though this point was not exclusively stated.<sup>44</sup> Kim et al.<sup>23</sup> reported the synthesis of a novel mesoporous  $\text{Zr-WO}_x/\text{SiO}_2$  catalyst via a soft-templating method. By using this technique the authors selectively deposited  $\text{Zr-WO}_x$  clusters, having different but controllable W/Zr ratios, within the  $\text{SiO}_2$  framework. It was demonstrated from this work that the sample with a W/Zr ratio of 0.3 had the strongest Brønsted acidity and highest catalytic activity for the esterification of 1-butanol with acetic acid.

The post-impregnation experiment and the new synthetic routes that have recently been reported demonstrate that a superior catalyst with a higher Zr-WO<sub>x</sub> cluster density can indeed be intentionally and deliberately engineered.

#### 4. FUTURE PROSPECTS: IN SITU IMAGING AND CATALYSTS BY DESIGN

The application of advanced characterization techniques, such as in situ optical spectroscopy and aberration corrected scanning transmission electron microscopy, has substantially improved our understanding of the relationship between the molecular/electronic structure and the catalytic performance of WO<sub>x</sub>/ZrO<sub>2</sub> catalysts. By using aberration corrected electron microscopy, it was possible to directly identify and distinguish different WO<sub>x</sub> surface species down to subnanometer resolutions, which when combined with deductions from in situ optical spectroscopy, allowed us to extract useful information that informed the development of a more cohesive structure–activity correlation model.

It is important to realize that new opportunities are continually arising for applying newly developed in situ characterization techniques that can reveal detailed information on the true nature of the active site(s) in various catalytic systems. For example recent improvements in in situ aberration corrected electron microscopy now allows atomic resolution imaging to be performed at elevated temperatures and under nonvacuum environments.<sup>105,106</sup> Such in situ real-space direct imaging, in combination with the rich structural information provided by in situ optical<sup>107</sup> spectroscopy, can potentially provide an unprecedented understanding of how such catalysts function at the atomic scale.<sup>108</sup>

A better understanding of the structure–catalytic activity relationship is essential in developing improved catalyst synthesis methods.<sup>23,28,45</sup> As has been demonstrated, a simple postimpregnation procedure can transform an inactive model WO<sub>3</sub>/ZrO<sub>2</sub> catalyst into a highly active catalyst by increasing its Zr-WO<sub>x</sub> cluster density. This concept applied to other novel synthesis approaches can lead to more sophisticated catalyst synthesis protocols for designing supported metal oxide catalysts with enhanced performance.

Advanced theoretical calculations have improved our fundamental understanding of the complex structure–activity correlations and can lead to critical improvements over current catalyst synthesis techniques. The experimental work reviewed in this article demonstrated that ZrO<sub>x</sub> species play a crucial role in the formation of the active sites (Zr-WO<sub>x</sub> clusters) but could not explain the specific effect of those species on the intrinsic cluster activity. Preliminary first-principles theoretical DFT calculations are starting to explain the role of ZrO<sub>x</sub> species (Zr<sup>4+</sup>) in lowering the deprotonation energy (or increasing the Brønsted acidity) of the WO<sub>x</sub> clusters. More informed theoretical studies of this type can further elucidate structure–activity correlations that can be exploited to rationally design experiments to test the validity of a hypothesized model and, hopefully, ultimately lead to better catalyst synthesis methods.

The supported WO<sub>3</sub>/ZrO<sub>2</sub> solid acid catalyst system featured in this perspective article provides an excellent example for showcasing how advanced characterization techniques, including optical spectroscopy and electron microscopy methods, coupled with state of the art theoretical calculations complement each other in providing new fundamental insights into the structure–activity relationship of an important oxide-on-oxide

catalyst system. These advanced characterization techniques, in combination with atomistic simulation and improved synthesis methods, will continue to help catalysis researchers to solve the workings of complex catalyst systems and make new discoveries when designing catalysts at the molecular and atomic level.

#### AUTHOR INFORMATION

Corresponding Author

\*E-mail for I.E.W.: [iew0@lehigh.edu](mailto:iew0@lehigh.edu).

ORCID 

Wu Zhou: 0000-0002-6803-1095

Michael S. Wong: 0000-0002-3652-3378

Present Addresses

#ExxonMobil Chemical Company, Global Process Research, 4500 Bayway Drive, Baytown, TX 77575, USA.

∇Department of Chemical Engineering and Materials Science, University of Minnesota, Minneapolis, MN 55455, USA.

Author Contributions

○These principal authors contributed equally to this work.

Notes

The authors declare no competing financial interest.

#### ACKNOWLEDGMENTS

We express our most sincere acknowledgment to our collaborators: E. I. Ross-Medgaarden, T. J. Kim, and W. V. Knowles. This work was sponsored by the National Science Foundation's Nanoscale Interdisciplinary Research Team (NSF-NIRT) program under grant #0609018. W.Z. acknowledges support from the CAS Pioneer Hundred Talents Program.

#### REFERENCES

- (1) Hino, M.; Arata, K. *J. Chem. Soc., Chem. Commun.* 1988, 1259–1260.
- (2) Karim, A. H.; Triwahyono, S.; Jalil, A. A.; Hattori, H. *Appl. Catal., A* 2012, 433–434, 49–57.
- (3) Rao Gijupalli, S.; Mugawar, S.; Rajan, P. N.; Balla, P. K.; Komandur, V. R. C. *Appl. Surf. Sci.* 2014, 309, 153–159.
- (4) Znaiguia, R.; Brandhorst, L.; Christin, N.; Baca, V. B.; Rey, P.; Millet, J.-M. M.; Loridant, S. *Microporous Mesoporous Mater.* 2014, 196, 97–103.
- (5) Foo, R.; Vazhnova, T.; Lukyanov, D. B.; Millington, P.; Collier, J.; Rajaram, R.; Golunski, S. *Appl. Catal., B* 2015, 162, 174–179.
- (6) Kantcheva, M.; Milanova, M.; Mametsheripov, S. *Catal. Today* 2012, 191, 12–19.
- (7) Wongmaneeil, P.; Jongsomjit, B.; Praserttham, P. *Catal. Lett.* 2010, 139, 42–49.
- (8) Ngaosuwan, K.; Jongsomjit, B.; Praserttham, P. *Catal. Lett.* 2010, 136, 134–140.
- (9) Senso, N.; Jongsomjit, B.; Praserttham, P. *Fuel Process. Technol.* 2011, 92, 1537–1542.
- (10) Yuan, P.-Q.; Liu, Y.; Bai, F.; Xu, L.; Cheng, Z.-M.; Yuan, W.-K. *Catal. Commun.* 2011, 12, 753–756.
- (11) Zhang, C.; Liu, T.; Wang, H.-J.; Wang, F.; Pan, X.-Y. *Chem. Eng. J.* 2011, 174, 236–241.
- (12) Wang, H.; Wu, Y.; He, L.; Liu, Z. *Energy Fuels* 2012, 26, 6518–6527.

- (13) Kourieh, R.; Bennici, S.; Marzo, M.; Gervasini, A.; Auroux, A. *Catal. Commun.* 2012, 19, 119–126.
- (14) Kourieh, R.; Rakic, V.; Bennici, S.; Auroux, A. *Catal. Commun.* 2013, 30, 5–13.
- (15) Giang, C.; Osatiashtiani, A.; dos Santos, V. C.; Lee, A. F.; Wilson, D. R.; Waldron, K. W.; Wilson, K. *Catalysts* 2014, 4, 414–426.
- (16) Kumar, A.; Ali, A.; Vinod, K. N.; Mondal, A. K.; Hegde, H.; Menon, A.; Thimmappa, B. H. S. *J. Mol. Catal. A: Chem.* 2013, 378, 22–29.
- (17) Poyraz, A. S.; Kuo, C.-H.; Kim, E.; Meng, Y.; Seraji, M. S.; Suib, S. L. *Chem. Mater.* 2014, 26, 2803–2813.
- (18) Chambon, F.; Rataboul, F.; Pinel, C.; Cabiac, A.; Guillon, E.; Essayem, N. *Appl. Catal., A* 2015, 504, 664–671.
- (19) dos Santos, V. C.; Wilson, K.; Lee, A. F.; Nakagaki, S. *Appl. Catal., B* 2016, 162, 75–84.
- (20) Ciptonugroho, W.; Al-Shaal, M. G.; Mensah, J. B.; Palkovits, R. J. *Catal.* 2016, 340, 17–29.
- (21) Hasan, Z.; Jeon, J.; Jung, S. H. *J. Hazard. Mater.* 2012, 205–206, 216–221.
- (22) Shringarpure, P. A.; Patel, A. *Dalton Trans.* 2010, 39, 2615–2621.
- (23) Kim, T. Y.; Park, D. S.; Choi, Y.; Baek, J.; Park, J. R.; Yi, J. J. *Mater. Chem.* 2012, 22, 10021–10028.
- (24) Signoretto, M.; Ghedini, E.; Menegazzo, F.; Cerrato, G.; Crocella, V.; Bianchi, C. L. *Microporous Mesoporous Mater.* 2013, 165, 134–141.
- (25) Zhu, J.; Tang, K.; Ye, Y.; Yuan, X.; Yang, W.; Tang, Y. *RSC Adv.* 2016, 6, 82537–82540.
- (26) Li, S.; Zhou, H.; Jin, C.; Feng, N.; Liu, F.; Deng, F.; Wang, J.-Q.; Huang, W.; Xiao, L.; Fan, J. *J. Phys. Chem. C* 2014, 118, 6283–6290.
- (27) Wang, P.; Feng, J.; Zhao, Y.; Wang, S.; Liu, J. *ACS Appl. Mater. Interfaces* 2016, 8, 23755–23762.
- (28) Song, K.; Zhang, H.; Zhang, Y.; Tang, Y.; Tang, K. J. *Catal.* 2013, 299, 119–128.
- (29) Praserttham, S.; Wongmaneevil, P.; Jongsomjit, B. *J. Ind. Eng. Chem.* 2010, 16, 935–940.
- (30) Del Angel, P.; Hernandez-Pichardo, M. L.; Montoya de la Fuente, J. A. *Catal. Today* 2013, 212, 201–205.
- (31) Yamamoto, T.; Teramachi, A.; Orita, A.; Kurimoto, A.; Motoi, T.; Tanaka, T. *J. Phys. Chem. C* 2016, 120, 19705–19713.
- (32) Osiglio, L.; Sathicq, A. G.; Romanelli, G. P.; Blanco, M. N. *J. Mol. Catal. A: Chem.* 2012, 359, 97–103.
- (33) Song, Y.; Zhang, J.; Zhang, Y.; Zhou, X.; Wang, J.-A.; Xu, L. *Catal. Today* 2011, 166, 79–83.
- (34) Kaucky, D.; Wichterlova, B.; Dedecek, J.; Sobalik, Z.; Jakubec, I. *Appl. Catal., A* 2011, 397, 82–93.
- (35) Song, Y.; Zhang, J.; Zhou, X.; Wang, J.-A.; Xu, L.; Yu, G. *Catal. Today* 2011, 166, 67–72.
- (36) Scheithauer, M.; Cheung, T. K.; Jentoft, R. E.; Grasselli, R. K.; Gates, B. C.; Knözinger, H. *J. Catal.* 1998, 180, 1–13.
- (37) Barton, D. G.; Soled, S. L.; Meitzner, G. D.; Fuentes, G. A.; Iglesia, E. *J. Catal.* 1999, 181, 57–72.
- (38) Barton, D. G.; Shtein, M.; Wilson, R. D.; Soled, S. L.; Iglesia, E. *J. Phys. Chem. B* 1999, 103, 630–640.
- (39) Baertsch, C. D.; Soled, S. L.; Iglesia, E. *J. Phys. Chem. B* 2001, 105, 1320–1330.
- (40) Baertsch, C. D.; Komala, K. T.; Chua, Y.-H.; Iglesia, E. *J. Catal.* 2002, 205, 44–57.
- (41) Macht, J.; Baertsch, C. D.; May-Lozano, M.; Soled, S. L.; Wang, Y.; Iglesia, E. *J. Catal.* 2004, 227, 479–491.
- (42) Wachs, I. E.; Kim, T.; Ross, E. I. *Catal. Today* 2006, 116, 162–168.
- (43) Kim, T.; Burrows, A.; Kiely, C. J.; Wachs, I. E. *J. Catal.* 2007, 246, 370–381.
- (44) Ross-Medgaarden, E. I.; Knowles, W. V.; Kim, T.; Wong, M. S.; Zhou, W.; Kiely, C. J.; Wachs, I. E. *J. Catal.* 2008, 256, 108–125.
- (45) Zhou, W.; Ross-Medgaarden, E. I.; Knowles, W. V.; Wong, M. S.; Wachs, I. E.; Kiely, C. J. *Nat. Chem.* 2009, 1, 722–728.
- (46) Soultanidis, N.; Zhou, W.; Psarras, A. C.; Gonzalez, A. J.; Iliopoulou, E. F.; Kiely, C. J.; Wachs, I. E.; Wong, M. S. *J. Am. Chem. Soc.* 2010, 132, 13462–13471.
- (47) Ross-Medgaarden, E. I.; Wachs, I. E. *J. Phys. Chem. C* 2007, 111, 15089–15099.
- (48) Ross, E. I. Ph.D. Thesis, Lehigh University, 2007.
- (49) Zhou, W.; Ross-Medgaarden, E.; Wachs, I.; Kiely, C. *Microsc. Microanal.* 2008, 14, 1350–1351.
- (50) Iglesia, E.; Barton, D. G.; Soled, S. L.; Miseo, S.; Baumgartner, J. E.; Gates, W. E.; Fuentes, G. A.; Meitzner, G. D. *Stud. Surf. Sci. Catal.* 1996, 101, 533–542.
- (51) Yori, J. C.; Pieck, C. L.; Parera, J. M. *Appl. Catal., A* 1999, 181, 5–14.
- (52) Wang, S.; Murata, K.; Hayakawa, T.; Hamakawa, S.; Suzuki, K. *Catal. Lett.* 2000, 66, 13–17.
- (53) Grau, J. M.; Yori, J. C.; Parera, J. M. *Appl. Catal., A* 2001, 213, 247–257.
- (54) Miyaji, A.; Echizen, T.; Li, L.; Suzuki, T.; Yoshinaga, Y.; Okuhara, T. *Catal. Today* 2002, 74, 291–297.
- (55) Scheithauer, M.; Jentoft, R. E.; Gates, B. C.; Knözinger, H. *J. Catal.* 2000, 191, 271–274.
- (56) Barton, D.; Soled, S.; Iglesia, E. *Top. Catal.* 1998, 6, 87–99.
- (57) Santiesteban, J. G.; Vartuli, J. C.; Han, S.; Bastian, R. D.; Chang, C. D. *J. Catal.* 1997, 168, 431–441.
- (58) Lebarbier, V.; Clet, G.; Houalla, M. *J. Phys. Chem. B* 2006, 110, 13905–13911.
- (59) Lopez, D. E.; Suwannakarn, K.; Bruce, D. A.; Goodwin, J. G., Jr. *J. Catal.* 2007, 247, 43–50.
- (60) Boudart, M. *Kinetics of heterogeneous catalytic reactions*; Princeton University Press: Princeton, NJ, 1984.
- (61) International Union of Pure and Applied Chemistry. *Compendium of Chemical Terminology*; Blackwells: Oxford, U.K., 1997.
- (62) Boyse, R. A.; Ko, E. I. *J. Catal.* 1997, 171, 191–207.
- (63) Vaidyanathan, N.; Houalla, M.; Hercules, D. M. *Catal. Lett.* 1997, 43, 209–212.
- (64) Ferraris, G.; De Rossi, S.; Gazzoli, D.; Pettiti, I.; Valigi, M.; Magnacca, G.; Morterra, C. *Appl. Catal., A* 2003, 240, 119–128.
- (65) Di Gregorio, F.; Keller, V. *J. Catal.* 2004, 225, 45–55.
- (66) Diaz, A. L.; Bussell, M. E. *J. Phys. Chem.* 1993, 97, 470–477.
- (67) Bond, G. C.; Flamerz, S.; Shukri, R. *Faraday Discuss. Chem. Soc.* 1989, 87, 65–77.
- (68) Knowles, W. V.; Nutt, M. O.; Wong, M. S. In *Handbook of Catalyst Synthesis: The Science and Engineering of Catalyst*; Regalbuto, J. R., Ed.; Taylor and Francis: Abingdon, U.K., 2007; pp 251–281.
- (69) Herzing, A. A.; Kiely, C. J.; Carley, A. F.; Landon, P.; Hutchings, G. J. *Science* 2008, 321, 1331–1335.
- (70) Caruthers, J. M.; Lauterbach, J. A.; Thomson, K. T.; Venkatasubramanian, V.; Snively, C. M.; Bhan, A.; Katare, S.; Oskarsdottir, G. *J. Catal.* 2003, 216, 98–109.
- (71) Furdal, K. L.; Tilley, T. D. *J. Catal.* 2003, 216, 265–275.
- (72) Saito, S.; Yamamoto, H. *Acc. Chem. Res.* 2004, 37, 570–579.
- (73) Hutchings, G. J. *J. Mater. Chem.* 2009, 19, 1222–1235.
- (74) Nørskov, J. K.; Bligaard, T.; Rossmeis, J.; Christensen, C. H. *Nat. Chem.* 2009, 1, 37–46.
- (75) Neurock, M. *J. Catal.* 2003, 216, 73–88.
- (76) Knözinger, H. In *Surface Chemistry in Biomedical and Environmental Science*; Blitz, J., Gun'ko, V., Eds.; Springer: Berlin, 2006; Vol. 228, pp 349–358.
- (77) Vartuli, J. C.; Santiesteban, J. G.; Traverso, P.; Cardona-Martinez, N.; Chang, C. D.; Stevenson, S. A. *J. Catal.* 1999, 187, 131–138.
- (78) Satsuma, A.; Yokoi, H.; Nishiyama, H.; Kakimoto, S.; Sugaya, S.; Oshima, T.; Hattori, T. *Chem. Lett.* 2004, 33, 1250–1251.
- (79) Cortés-Jacome, M. A.; Angeles-Chavez, C.; Lopez-Salinas, E.; Navarrete, J.; Toribio, P.; Toledo, J. A. *Appl. Catal., A* 2007, 318, 178–189.
- (80) Cortés-Jacome, M. A.; Angeles-Chavez, C.; Bokhimi, X.; Toledo-Antonio, J. A. *J. Solid State Chem.* 2006, 179, 2663–2673.

- (81) Raveendran Shiju, N.; Yoshida, K.; Boyes, E. D.; Robert Brown, D.; Gai, P. L. *Catal. Sci. Technol.* 2011, 1, 413–425.
- (82) Kim, Y. K.; Rousseau, R.; Kay, B. D.; White, J. M.; Dohnalek, Z. *J. Am. Chem. Soc.* 2008, 130, 5059–5061.
- (83) Tang, X.; Bumüller, D.; Lim, A.; Schneider, J.; Heiz, U.; Gantefoer, G.; Fairbrother, D. H.; Bowen, K. H. *J. Phys. Chem. C* 2014, 118, 29278–29286.
- (84) Wilson, R. D.; Barton, D. G.; Baertsch, C. D.; Iglesia, E. *J. Catal.* 2000, 194, 175–187.
- (85) Weber, R. S. *J. Catal.* 1995, 151, 470–474.
- (86) Kuba, S.; Lukinskas, P.; Grasselli, R. K.; Gates, B. C.; Knözinger, H. *J. Catal.* 2003, 216, 353–361.
- (87) Nakka, L.; Molinari, J. E.; Wachs, I. E. *J. Am. Chem. Soc.* 2009, 131, 15544–15554.
- (88) Molinari, J. E.; Nakka, L.; Kim, T.; Wachs, I. E. *ACS Catal.* 2011, 1, 1536–1548.
- (89) Calabro, D. C.; Vartuli, J. C.; Santiesteban, J. G. *Top. Catal.* 2002, 18, 231–242.
- (90) Zhou, W.; Wachs, I. E.; Kiely, C. J. *Curr. Opin. Solid State Mater. Sci.* 2012, 16, 10–22.
- (91) Farneth, W. E.; Gorte, R. J. *Chem. Rev.* 1995, 95, 615–635.
- (92) Sauer, J. *Chem. Rev.* 1989, 89, 199–255.
- (93) Vansanten, R. A.; Kramer, G. J. *Chem. Rev.* 1995, 95, 637–660.
- (94) Bardin, B. B.; Bordawekar, S. V.; Neurock, M.; Davis, R. J. *J. Phys. Chem. B* 1998, 102, 10817–10825.
- (95) Carr, R. T.; Neurock, M.; Iglesia, E. *J. Catal.* 2011, 278, 78–93.
- (96) Janik, M. J.; Davis, R. J.; Neurock, M. *Catal. Today* 2005, 105, 134–143.
- (97) Janik, M. J.; Macht, J.; Iglesia, E.; Neurock, M. *J. Phys. Chem. C* 2009, 113, 1872–1885.
- (98) Knaeble, W.; Carr, R. T.; Iglesia, E. *J. Catal.* 2014, 319, 283–296.
- (99) Macht, J.; Carr, R. T.; Iglesia, E. *J. Catal.* 2009, 264, 54–66.
- (100) Macht, J.; Janik, M. J.; Neurock, M.; Iglesia, E. *J. Am. Chem. Soc.* 2008, 130, 10369–10379.
- (101) Xu, J.; Zheng, A. M.; Yang, J.; Su, Y. C.; Wang, J. Q.; Zeng, D. L.; Zhang, M. J.; Ye, C. H.; Deng, F. *J. Phys. Chem. B* 2006, 110, 10662–10671.
- (102) Gounder, R.; Iglesia, E. *Angew. Chem., Int. Ed.* 2010, 49, 808–811.
- (103) Gounder, R.; Iglesia, E. *Acc. Chem. Res.* 2012, 45, 229–238.
- (104) Jones, A. J.; Iglesia, E. *ACS Catal.* 2015, 5, 5741–5755.
- (105) de Jonge, N.; Bigelow, W. C.; Veith, G. M. *Nano Lett.* 2010, 10, 1028–1031.
- (106) Hansen, P. L.; Wagner, J. B.; Helveg, S.; Rostrup-Nielsen, J. R.; Clausen, B. S.; Topsøe, H. *Science* 2002, 295, 2053–2055.
- (107) Bluhm, H.; Havecker, M.; Knop-Gericke, A.; Kiskinova, M.; Schlögl, R.; Salmeron, M. *MRS Bull.* 2007, 32, 1022–1030.
- (108) Behrens, M.; Studt, F.; Kasatkin, I.; Kühl, S.; Havecker, M.; Abild-Pedersen, F.; Zander, S.; Girgsdies, F.; Kurr, P.; Kniep, B.-L.; Tovar, M.; Fischer, R. W.; Nørskov, J. K.; Schlögl, R. *Science* 2012, 336, 893–897.